

Ocean & Sea Ice SAF

Global Sea Ice Edge and Type Algorithm Theoretical Basis Document

GBL SIE OSI-402-c and GBL SIT OSI-403-c

Version 2.2 — May 2016

Signe Aaboe, Lars-Anders Breivik and Steinar Eastwood
Norwegian Meteorological Institute

The EUMETSAT
Network of
Satellite Application
Facilities



OSI SAF
Ocean and Sea Ice

Documentation Change Record:

Version	Date	Author	Description
1.0	18.11.2013	SAA	First version
1.1	27.02.2014	SAA	Updated after review. Added validation results ++.
1.2	10.04.2015	SAA	Included more details on dynamical PDF's.
2.0	15.12.2015	SAA	Introduction of Metop-B ASCAT, F18 SSMIS and GW1 AMSR-2 submitted for PCR: chapter 2, section 3.6-3.7, 4.1.
2.1	31.01.2016	SAA	Updated according to comments from PCR review.
2.2	30.05.2016	SAA	Updated figures in Sec 4.1.1. SSMIS from F17 are not used since the 12th of April, 2016.

Table of contents

Table of contents

Glossary	2
1 Introduction	1
1.1 The EUMETSAT Ocean and Sea Ice SAF	1
1.2 Scope	1
1.3 Overview	1
2 Input data	3
2.1 Passive microwave data	3
2.1.1 Atmospheric corrections	5
2.2 Scatterometer data	5
2.3 Data summary	6
3 Algorithm description	8
3.1 Bayesian approach for sea ice classification	8
3.2 Ice classes and training data	9
3.3 Dynamical PDF's	10
3.3.1 Choice of the period length for statistical analyze	11
3.3.2 Interannual variability of dynamical PDF's	13
3.3.3 Manual control on target areas	13
3.4 Scatterometer ice detection	13
3.5 PMW ice detection	18
3.6 Multi-sensor ice edge analysis, OSI-402-c	21
3.7 Multi-sensor ice type analysis, OSI-403-c	23
4 Preliminary Validation and Technical Issues	25
4.1 Preliminary validation results	25
4.1.1 Time series of PDF's from new satellites versus operational ones	25
4.1.2 Inclusion of ASCAT from Metop-B	31
4.1.3 Switch to SSMIS from F18	31
4.1.4 Inclusion of AMSR2 data	31
4.2 Exception handling	36
4.2.1 Missing input data	36
4.3 Assumptions and Limitations	36
4.3.1 Assumption on distribution type	36
4.3.2 Limitation on ice type product period	36
4.3.3 No ice type classification on Southern Hemisphere	36

A Time series of PDF's - dynamical versus static	37
B Flow charts	45
References	48

Glossary

SSMIS	Special Sensor Microwave Imager/Sounder.
AMSR2	Advanced Microwave Scanning Radiometer 2.
ASCAT	Advanced Scatterometer.
AVHRR	Advanced Very High Resolution Radiometer.
DMI	Danish Meteorological Institute.
DMSP	Defense Meteorological Satellite Program.
ECMWF	European Center for Medium-Range Weather Forecasts.
EUMETSAT	European Organization for the Exploitation of Meteorological Satellites.
FY	First Year (sea ice).
GCOM-W	Global Change Observation Mission for Water.
GW1	GCOM-W1.
HL	High Latitude.
JAXA	Japan Aerospace Exploration Agency.
MET-Norway	Norwegian Meteorological Institute.
Metop	Meteorological Operational polar satellite program.
MY	Multi Year (sea ice).
NOAA	National Oceanic and Atmospheric Administration.
NSIDC	National Snow and Ice Data Center.
NWP	Numerical Weather Prediction.
OSI SAF	Ocean and Sea Ice SAF.
OSI-401	OSI SAF Sea Ice Concentration product.
OSI-402	OSI SAF Sea Ice Edge product.
OSI-403	OSI SAF Sea Ice Type product.
PDF	Probability Distribution Function.
PMW	Passive Micro Wave.

RTM	Radiative Transfer Model.
SAF	Satellite Application Facility.
SAR	Synthetic Aperture Radar.
SMMR	Scanning Multichannel Microwave Radiometer.
SSM/I	Special Sensor Microwave/Imager.
STD	Standard deviation.
TB	Brightens Temperature.
WMO	World Meteorological Organization.

1. Introduction

1.1 The EUMETSAT Ocean and Sea Ice SAF

For complementing its Central Facilities capability in Darmstadt and taking more benefit from specialized expertise in Member States, EUMETSAT created Satellite Application Facilities (SAFs), based on co-operation between several institutes and hosted by a National Meteorological Service. More on SAFs can be read from www.eumetsat.int.

The Ocean and Sea Ice Satellite Application Facility (OSI SAF) is producing on an operational basis a range of air-sea interface products, namely: wind, sea ice characteristics, Sea Surface Temperatures, Surface Solar Irradiance and Downward Longwave Irradiance. The sea ice products include Sea Ice Concentration, Sea Ice Emissivity, Sea Ice Edge, Sea Ice Type, Sea Ice Drift, and latest also Sea Ice Surface Temperature (from mid-2014).

The OSI SAF consortium is hosted by Météo-France. The sea ice processing is performed at the High Latitude processing facility (HL centre), operated jointly by the Norwegian Meteorological Institute (MET-Norway) and Danish Meteorological Institute (DMI).

Note: The ownership and copyrights of the data set belong to EUMETSAT. The data is distributed freely, but EUMETSAT must be acknowledged when using the data. EUMETSAT's copyright credit must be shown by displaying the words "copyright (year) EUMETSAT" on each of the products used. User feedback to the OSI SAF project team is highly valued. The comments we get from our users is important argumentation when defining development activities and updates. We welcome anyone to use the data and provide feedback.

1.2 Scope

This document is dedicated to the OSI SAF product users and describes the scientific background of, and details in the OSI SAF global Sea Ice Edge (OSI-402-c) and Type (OSI-403-c) products.

1.3 Overview

The global Sea Ice Edge and Sea Ice Type products are both classification products that distinguish between the following classes:

- Sea Ice Edge (OSI-402 series) – distinguish between open water, open sea ice and closed sea ice
- Sea Ice Type (OSI-403 series) – distinguish between first-year ice and multi-year ice.

Both products are multi-sensor products derived from passive and active microwave remote sensing data combined in a Bayesian approach. They are computed for both hemispheres on the standard OSI SAF grid with 10 km spatial resolution.

In the start of the operational production in 2005 the development of the sea ice products used passive microwave data from SSM/I onboard the DMSP satellites. In 2009 ASCAT scatterometer data from Metop-A was introduced in the operational products of Ice Edge (OSI-402) and Ice Type (OSI-403). In 2013, the SSM/I data was replaced by SSMIS data from DMSP F17, and the products thereby changed label to OSI-402-a and OSI-403-a, respectively [Aaboe et al., 2013]. The two sea ice products improved in 2015 by introducing a dynamical training data set and changed label to OSI-402-b and OSI-403-b, respectively. For the present upgrade, OSI-402-c and OSI-403-c, the following new data are introduced to the analysis:

- ASCAT data from Metop-B, which for a period will run parallel with Metop-A.
- SSMIS data from F18, taking over for F17.
- AMSR2 from JAXA's GCOM-W1 is introduced as an additional sensor.

Note: At present the OSI SAF Sea Ice Type product delivered for Southern Hemisphere classify all sea ice as “ambiguous”. The reason for this is that there has still not been carried out enough studies for the Antarctica sea ice classes to do a Southern Hemisphere ice type classification. Similarly for the Northern Hemisphere, in the summer period from mid-May until mid-October the sea ice is classified as “ambiguous”. This is due to wet ice and melting ponds on the ice which makes it more difficult to distinguish between first-year ice and multi-year ice.

The scientific background and algorithm is described in detail in this document.

2. Input data

2.1 Passive microwave data

Satellite derived Passive MicroWave data (PMW) over the ocean has been the backbone of large scale sea ice monitoring with more than 30 years record. The Scanning Multichannel Microwave Radiometer (SMMR) on Nimbus-7 operated from 1978 until 1987. The Special Sensor Microwave/Imager (SSM/I) has been flown since 1987. The sensor on-board the DMSP F15 satellite was the last SSM/I sensor being used operational in the OSI SAF products. Its follower, the Special Sensor Microwave Imager/Sounder (SSMIS), has since 2013 replaced the use of SSM/I data. In the present upgrade, the SSMIS data from F18 is introduced in the OSI SAF ice edge and type analysis. The data from F17 stopped being used in April 2016 due to calibration problems, and F18 has therefore been used in the operational products since then (see [Aaboe et al., 2016]).

The Advanced Microwave Scanning Radiometer 2 (AMSR2) on-board the GCOM-W1 (GW1) satellite is a passive microwave radiometer similar to the SSM/I and SSMIS but with the larger differences of having a higher spatial resolution than SSM/I and SSMIS, see Table 1. For SSMIS the sampling interval is 25 km and 12.5 km for the two lower frequencies and the higher frequency, respectively, while for AMSR2 the corresponding grid sampling is 10 km and 5 km. Since 2016, AMSR2 data is introduced as a new sensor in the OSI SAF multi-sensor products of ice edge and type.

The SSM/I, SSMIS and AMSR2 imaging systems are all conical scanning, passive microwave radiometers, see the scanning geometry for SSMIS on Figure 1. The passive microwave radiometers measure the upwelling surface microwave brightness temperature (TB), which is linearly related to the physical surface temperature¹. For the OSI SAF ice products is used TB measurements at three different frequencies sampled in both horizontal and vertical polarization. The channel specifications for all sensors included in the OSI SAF sea ice edge and type products are given in Table 1 (SSM/I-F15 and SSMIS-F17 are included for comparison as being the last discontinued sensors). Note, that due to the smaller differences in the three frequencies between the sensor types, the higher frequency (85 GHz for SSMI, 91 GHz for SSMIS and 89 GHz for AMSR2) will in the following be referred to as the *near 90 GHz* or in short *N90*, while for the two lower resolutions we will in general just refer to *19* and *37 GHz*.

The measured emissivity from a calm ocean surface is strongly polarized and has generally low values. While for increasing surface roughness the emissivity also increases and additionally becomes less polarized. The emissivity of sea ice undergoes a complex transition while forming from open water and gradually thickening [Comiso, 1983]. First-year ice (FY), which is ice of approx. 0.1-2 m thickness that has not undergone a summer melt and freeze cycle, is characterized by a very high emissivity with low polarization. Multi-year ice (MY), i.e. ice that has survived at least one summer melt, is characterized by lower emissivity, declining with frequency, due to air pockets formed during the summer melt. To represent

¹Brightness temperature is defined as $TB = \epsilon T$, where ϵ is the microwave emissivity of the surface material and T is the physical surface temperature.

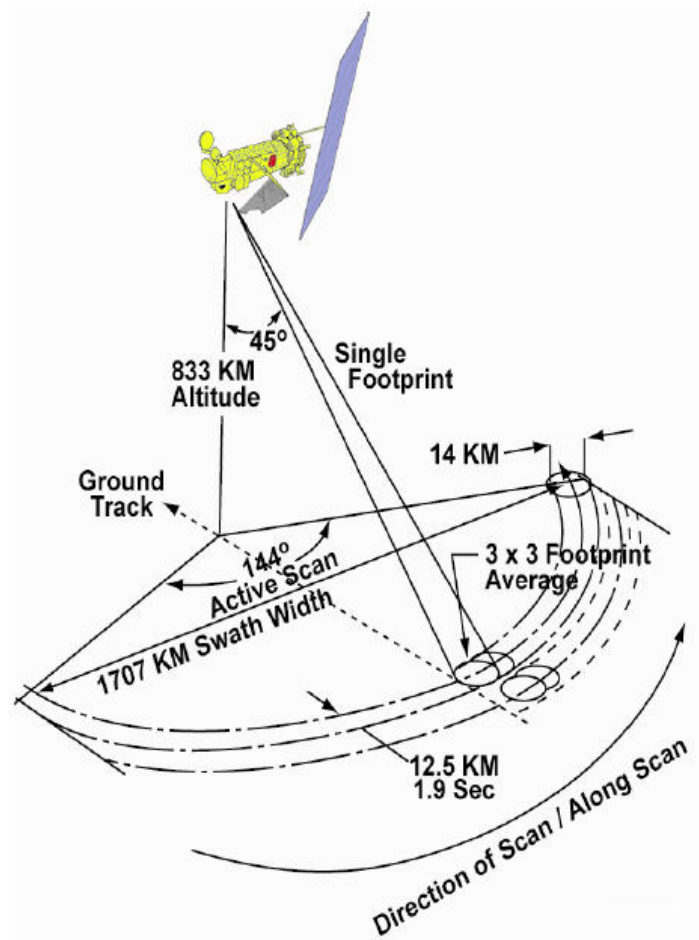


Figure 1: SSMIS scanning geometry, (source NSIDC web site)

these characteristics and to reduce the effects of the physical temperature, it is practical to define the Polarization Ratio (PR), which is the normalized difference between horizontal and vertical TB, and the spectral Gradient Ratio (GR), which is the normalized TB difference between two different frequencies:

$$\begin{aligned}
 PR_{19} &= [TB(19V) - TB(19H)] / [TB(19V) + TB(19H)] \\
 PR_{n90} &= [TB(N90V) - TB(N90H)] / [TB(N90V) + TB(N90H)] \\
 GR_{1937} &= [TB(19V) - TB(37V)] / [TB(19V) + TB(37V)]
 \end{aligned}
 \tag{2.1}$$

These parameters are derived from the measured TBs corrected for atmospheric influence (see Section 2.1.1). The variations in these characteristics are commonly used in algorithms to estimate ice concentration and distinguish between ice and water and different ice types, see e.g. Andersen [1998].

Sensor	Platform	Channels		Sampling [km]	Footprint size [km]	Last active date
		[GHz]	pol.			
SSMIS	F18	19.35	V,H	25	42x70	Active
		37.0	V,H	25	27x44	
		91.655	V,H	12.5	13x14	
ASCAT	Metop-A/ Metop-B	C band	VV	12.5	(25-34)x (25-34)	Active
AMSR2	GCOM-W1	18.7	V,H	10	14x22	Active
		36.5	V,H	10	7x12	
		89.0	V,H	5	3x5	
SSMIS	F17	19.35	V,H	25	42x70	07-04-2016
		37.0	V,H	25	27x44	
		91.655	V,H	12.5	13x14	
SSM/I	F15	19.35	V,H	25	43x69	03-10-2013
		37.0	V,H	25	28x37	
		85.5	V,H	12.5	13x15 km	

Table 1: Characteristics of the different sensors and channels used in the OSI SAF sea ice edge and type products.

2.1.1 Atmospheric corrections

Contamination arising from atmospheric water vapor content and wind roughening of the open water surface is a common problem in the remote sensing of sea ice from passive microwave observations. To mitigate this problem, a correction is computed using the radiative transfer model (RTM) by Wentz [1997] extended with a scheme developed by Kern [2004] for the 85 GHz channels, with numerical weather prediction (NWP) input from ECMWF model fields of surface wind, temperature and atmospheric water content. This correction is subsequently applied to the measured TBs as part of the OSI SAF sea ice concentration algorithm (OSI-401) prior to the calculation of the sea ice edge and type, so more details on the RTM is found in the OSI-401 ATBD [Tonboe and Lavelle, 2015, Section 4]. Given a mixture of weather contamination and low ice concentrations, such as often experienced in the marginal ice zone, the widely used threshold based weather filtering methods such as described by Cavalieri et al. [1995] tend to either remove the ice completely or leave it untouched. The NWP model based correction method will tend to only remove the weather-induced part and give more accurate concentration estimates. Note, that this method works directly on TB and is therefore well suited for use in both the ice edge and type products as well as for the ice concentration product.

2.2 Scatterometer data

The use of scatterometer data in the OSI SAF sea ice analysis started with the C-band radar scatterometers on-board the research satellites ERS-1 and -2 (1991-2011) designed and operated to deliver ocean surface wind vectors. In 2009, the Advanced SCATterometer (ASCAT) instrument on-board the Metop-A satellite was introduced operationally in the OSI

SAF sea ice edge and type products, and since the beginning of 2016 the ASCAT data from Metop-B is also included. In the overlap period of Metop-A and Metop-B, the ASCAT data from both satellites will be used for the ice products hereby contributing to a better coverage of data.

The scatterometer instrument measures the microwave backscatter, σ_0 , which have been averaged and re-sampled by using a Hamming window across and along the viewing swath in order to achieve spatial resolution and to reduce measurement noise [ASCAT Product Guide, 2015]. The microwave backscatter from the ocean surface and depends on the surface roughness, caused by for example the wind induced gravity/capillary waves over the ocean. The microwave backscatter over sea ice is dependent on the ice surface roughness and on the degree of volume scattering from brine pockets within the ice. Since the multi-year ice is often rougher than first-year, and since multi-year ice also has an additional backscatter signature as a result of volume scattering compared to first-year ice, the scatterometer backscatter measurements can be used to classify ice types [see e.g. Gohin and Cavanié, 1994].

The ASCAT measurement geometry is illustrated on Figure 2. Two sets of three antennas are used to generate radar beams oriented at 45° , 90° and 135° with respect to the satellite's flight direction, on both sides of the satellite ground track. Each of the beams cover 550 km-wide swaths as the satellite moves along its orbit. Sampling resolution is 25 km or 12.5 km which divides each swath into 21 or 42 cells, respectively. For each cell, three independent backscatter measurements, $\sigma_{0,fore}$, $\sigma_{0,mid}$ and $\sigma_{0,back}$, are obtained using the different viewing directions from the three antennas. The forward and backward pointing antennas are viewing the same cell on the ground with different viewing azimuths, but with the same incident angle. The mid antenna is viewing with a steeper incident angle. The variation in backscatter measurements due to the viewing geometry can be utilized to detect sea ice, following Cavanie et al. [1993]. First, backscattering is relatively isotropic over sea ice compared to the strong anisotropic behavior over open water. Secondly, the change of backscatter with incidence angle shows larger variation over water than over sea ice. The measure of the anisotropy, the *anisotropy coefficient* (*anisFB*), and the change of backscatter with incidence angle (*dsigma*) were proposed by Cavanie et al. [1993] for ice/water discrimination and is the basis for the method developed for ice/water discrimination under the OSI SAF (see more details in Section 3.4).

2.3 Data summary

Below in Table 2 is summarized the input data which in the present ATBD are suggested to be included in the next operational version of the sea ice edge and -type products.

Sensor	Variable [Units]	Level	Owner/Distributor	Format
SSMIS	TB [K]	1	NOAA/EUMETCast	BUFR
AMSR2	TB [K]	1	JAXA/GCOM-W1– Data Providing Service	HDF5
ASCAT	σ_0 (Hamming) [dB]	1	EUMETSAT/EUMETCast	BUFR

Table 2: Input data used in the OSI SAF sea ice edge and type products.

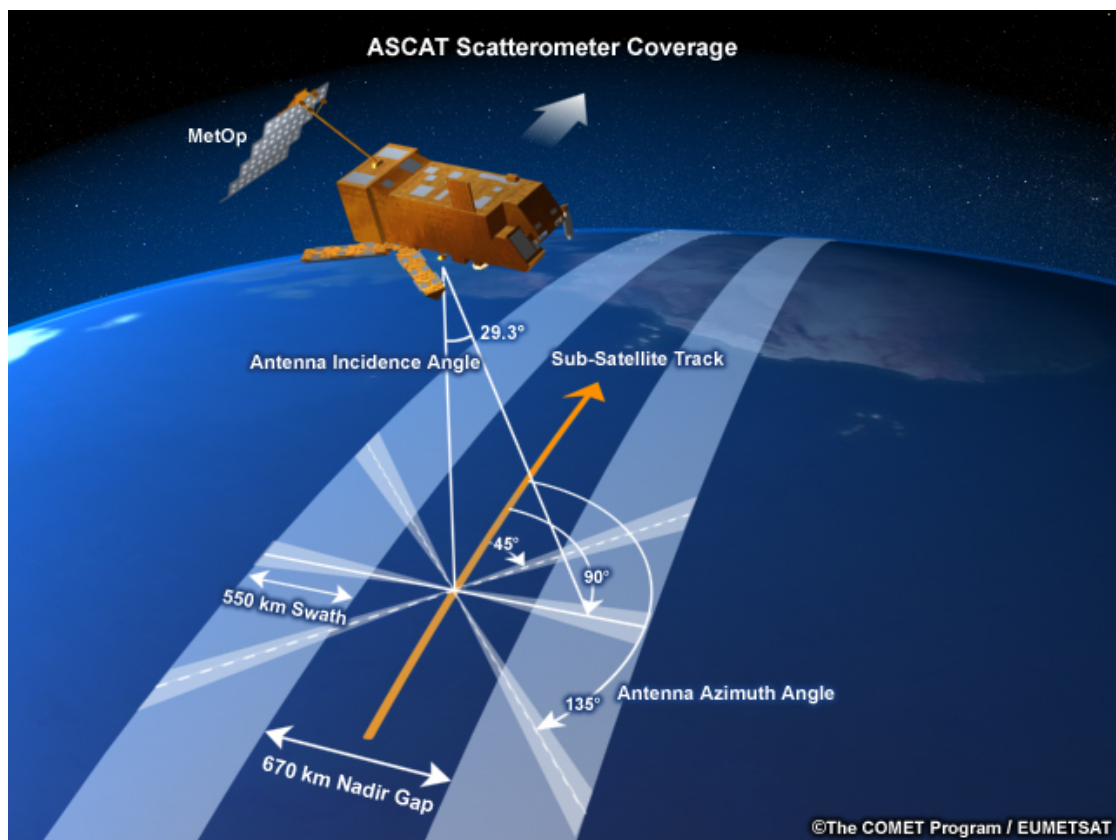


Figure 2: ASCAT geometry, (source COMET/EUMETSAT)

3. Algorithm description

In this section the algorithm for sea ice edge and type is described. An overview of the different processing steps is seen in Appendix B.

3.1 Bayesian approach for sea ice classification

A general tool for combining various data sources is given by the Bayesian (inverse method) approach. Using this approach, several measured parameters can be combined to derive the most likely estimate of e.g. the surface type. The approach is based on pre-knowledge of the averaged relationship (and scatter) between each surface type and the measured parameter. This knowledge can be expressed as a probability density distribution for the measured parameter *given the surface type*. For simplicity, if we allow for two surface types: *ice* and *water*, and a single measured parameter A , then an algorithm for ice edge detection can be derived. For this we need to know the probability of a measurement knowing that there is ice, $p(A|ice)$, and the probability of a measurement knowing that there is water, $p(A|water)$. Setting both the a-priori probabilities for ice and water, $P(ice)$ and $P(water)$, equal to 50%, the Bayesian approach simplifies to an expression of the probability for having ice given the measurement :

$$p(ice|A) = \frac{p(A|ice)}{p(A|ice) + p(A|water)} \quad (3.1)$$

The method can be generalized for combining several measured parameters e.g. from different satellite sensors to an optimal surface type estimate. Assume that we have n measured parameters A_1, A_2, \dots, A_n , which are independent and related to surface type. A general expression for the probability of a surface type I_k given the measured parameters is then given as:

$$p(I_k|A_1, \dots, A_n) = \frac{p(A_1|I_k) \cdot p(A_2|I_k) \cdot \dots \cdot p(A_n|I_k)}{\sum_j p(A_1|I_j) \cdot \dots \cdot p(A_n|I_j) P(I_j)} P(I_k) \quad (3.2)$$

The method works in such a way that the measured parameter, which the statistics show to be the most secure in distinguishing between surface types, is the one that gives most impact on the resulting probability estimate. Further, the method not only provides an estimate of the most probable surface type, but also of the uncertainty of this estimate. These benefits make the Bayesian method attractive compared to other methods based on threshold levels. In order to obtain the estimates of the averaged relationships, terms like e.g. $p(A|ice)$ and $p(A|water)$, we need a large training data set with measurements of A over known ice and open water conditions (see Section 3.2). In addition, we assume a Gaussian probability distribution of the averaged relationships, so that $p(A|I) \approx \frac{1}{\sigma} \exp(-\frac{(A-\mu)^2}{2\sigma^2})$, where μ and σ are the mean and the standard deviation of A , respectively, over a certain surface type I . μ and σ are found from the training data set. The a-priori probabilities, $P(I)$, in Eq. 3.2 for the different ice classes are set to be equal.

3.2 Ice classes and training data

The term ice edge is not an absolute quantity and depends on e.g. the spatial scale of interest. In general it can be defined as the demarcation at any given time between open water and sea. On very small scale it is the demarcation between an ice flake and open water. On larger scale it can be defined as the limit between *ice infested* water and open water, however this is a relative term. On the scales we are dealing with here, ice concentration is a well established parameter which can help to define the ice edge. A threshold in ice concentration of 15% is often used to define ice extent location in scientific studies and climate applications in order to eliminate unrealistic values caused by the influence of wind and weather in the near-open ocean region. In operational sea ice charting *ice classes* are defined according to established practice in the Ice Service community and as defined by the WMO sea ice nomenclature terminology, which is found in the WMO publication No. 259, Suppl. No. 4 on Sea Ice Nomenclature. Following this terminology the relationship between ice classes and ice concentration ranges are shown in Table 3.

Ice service class	Concentration range	Sea Ice Edge class
Open water	less than 1/10	Open water
Very open drift ice	1/10 - 4/10	Open water / open ice
Open drift ice	4/10 - 7/10	Open ice
Closed drift ice	7/10 - 9/10	Closed ice
Fast ice	More than 9/10	Closed ice

Table 3: Correspondence between sea ice classes as used by operational Sea Ice Services, ice concentration range and the sea ice class chosen for the OSI SAF ice edge classification.

Scatterometer data is not suitable for quantitatively determination of ice concentrations but can be used to discriminate between water and ice, and to a certain extent between open and closed ice. In the multi sensor ice edge product, OSI-402, this ice/water discrimination capability in ASCAT data is exploited. In combination with PMW *PRn90*, the intention is to provide a more detailed ice edge estimate compared to a plain PMW ice concentration product (OSI-401).

The first step in building the analysis system based on the Bayesian approach (Eq. 3.2) is to derive the probability density functions (PDF's) for each measured quantity given the ice class. In order to obtain the average and standard deviation of the expected measurement values, large training data sets from each of the sensors used in the analysis (at present that consists of ASCAT from Metop-A and -B, SSMIS from F18 and AMSR2 from GCOM-W1) are collocated with background sea ice information from a set of target areas that has been defined in the Arctic and the Antarctic. For ice edge classification target data with ice concentration¹ between 70% and 30%, i.e. mainly in the *open drift ice* regime, is defined as *open ice*. Ice concentrations below 30% is set to represent *open water*. And concentrations above 70% represent the *closed ice*. To differentiate between MY and FY ice in the Arctic, a sector north of Greenland and Canada between 30 W and 120 W are defined as MY while data from the Kara Sea, Baffin Bay, Laptev Sea and Bay of Bothnia are defined as FY

¹For ice concentration is used the OSI-401 product.

(see Figure 3). No ice type targets are defined in the Southern Hemisphere since Southern Hemisphere ice type, at present, is not classified in OSI SAF.

From the training data we get two sets of PDF's – one set for the Arctic which is based on data from NH, and one for Antarctica which is based on data from SH.

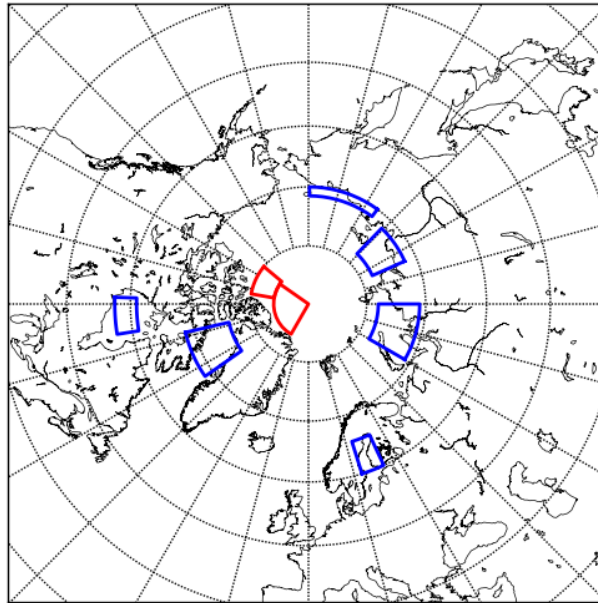


Figure 3: Target areas (per December 2015) in the Arctic used to analyze the behavior of satellite measurements over known ice types. Blue targets are defined for FY ice and red targets are for MY ice.

3.3 Dynamical PDF's

The sea ice properties influencing the measurements vary over the seasons. The PDF's representing the average relationships therefore also need to vary over the seasons. To achieve this the statistics are derived continuously throughout the year. In a previous version of the algorithm (OSI-402-a and OSI-403-a), the training data set was based on one fixed year of observations, March 2007 to February 2008. To account for seasonal variations the statistics were derived for each month of that year, individually. These monthly PDF's are referred to as the static PDF's.

In the current version of the algorithm, the statistics are derived daily based on a training data set continuously updated from the preceding 15 days. So, instead of using static PDF's originating from one year of data, the algorithm is now operated with **dynamical PDF's**. This is in principle the same method which is used for the OSI SAF sea ice concentration re-processing project which are using dynamical tie points to produce a climate consistent

time series based on data from the DMSP satellites between 1979 and 2009 [Eastwood et al., 2011]. Dynamical PDF's are introduced for two reasons:

1. To account for new sensors.

In the operational satellites programs the satellites are regularly renewed and replaced. ASCAT-Metop-C is following ASCAT-Metop-A/B and SSMIS-F18 follows SSMIS-F17. The instruments are the same or similar, but the performance of the algorithms need to be checked and tuned. The statistics derived from Metop-A and from F17 is likely to give quite good results also with the following instruments, but small changes might be expected and need to be taken into account. Instead of recalculating the statistics for one year and use this for the new instrument, *dynamic PDF's* allows for a smooth transition between the instruments.

2. To account for sea ice variations from different years.

Ice properties may also vary from year to year largely depending on the weather conditions in particular on the start and end of the melting and freezing seasons.

3.3.1 Choice of the period length for statistical analyze

Ideally the time period of the training data should be as short as possible to best represent the actual ice condition, however the length is also determined by the need to collect enough training data to derive reliable statistics. Test studies where the dynamic PDF's were estimated on periods of 10 days or shorter gave noisy PDF's. Whereas using periods of 20 days gave smooth PDF's however missing the changes in ice conditions which occurs over relatively short periods in transition from summer to winter and vice verse. This is seen in Figure 4, which show examples of using different period lengths when estimating the statistical means of the two parameters *anisFMB* (from ASCAT, defined in Eq. 3.4) and *PRn90* (from SSM/I, defined in Eq. 2.1), respectively. Also, when the statistics are based on observations *back* in time, a too long training period will be less representative for the actual day of ice calculations. Based on these considerations it has been chosen that on a daily basis dynamical PDF's are estimated from a training data set consisting of the last 15 days of observations.

It may happen, however, that in some 15-days periods there is not enough observations for some or for all targets for carrying out the statistical calculations. Typically this occurs during the summer months where ice is melting or is transformed into MY which can cause little or no observations over FY ice. In such cases, the algorithm will search for data in an increasing period until enough observations are found for the statistics.

For the special case where targets are completely missing within the 15-days period, the algorithm uses the static PDF's instead.

(a) ASCAT anisFMB (cell 15, Arctic)



(b) SSM/I PRn90 (Arctic)



Figure 4: Mean values of (a) ASCAT anisFMB and (b) SSM/I PRn90, used for the dynamical PDF's. Different period lengths, red: 5 days, green: 10 days, blue: 15 days, cyan: 20 days. In both (a) and (b), upper panel: *closed ice*, lower panel: *open water*.

3.3.2 Interannual variability of dynamical PDF's

In Appendix A is shown the dynamical PDF's based on ASCAT–Metop-A and SSMIS–F17. Figures A.1-A.4 show the time-series (2010-2014) of the daily dynamical PDF's for the parameters used for the ice edge algorithm, and Figures A.5-A.6 are for parameters used for the ice type algorithm - all for the Northern Hemisphere. For each parameter there is one plot for each year in addition to one plot for the corresponding static monthly PDF's. In general the dynamical PDF has a common seasonal behavior from year to year and is comparable with its corresponding static PDF. However there are some clear changes in the PDF's, especially during the summer month where onset of surface melting changes the PDF's for both ice edge and -type. In Figure A.7 is shown the corresponding dynamical PDF's for 2014 in the Southern Hemisphere.

For the ice type product (Figures A.5-A.6) it is seen that the PDF's for FY and MY often overlap in the period between end of May and start of October, with some year-to-year variability. The static PDF's also have a very high standard deviation during this period, which is set on purpose to assure that the algorithm classifies these periods as *ambiguous* ice class. In addition the PDF's for FY are seen to be largely effected by too few data during late summer. This is seen as constant values of the FY-PDF, since the algorithm tries to find more data by extending the period back in time. A consequence, of both the overlapping and the unsure FY-PDF's, is that during the summer months the OSI SAF gives no information on ice type in the data. The ice type is classified as *ambiguous* in this period. At present this period is defined from mid-May until mid-October.

3.3.3 Manual control on target areas

In the process of converting from static to dynamical PDF's the definition of the target areas for FY and MY ice was changed slightly. The present target definition is seen in Figure 3. The reason for this new target definition was due to recent maximum extent in MY ice. These MY maxima can occur when part of the FY ice survives the summer and thereby becomes second-year ice ([see e.g. news on [www: Reporting Climate Science](http://www.ReportingClimateScience.com), 2014]. If MY ice enters the target regions defined as FY this will give misleading ice classification results.

Every summer around the time of sea ice extent minimum, the OSI SAF sea ice team will do a manual monitoring of the definition of the target areas in order to see if it needs to be adjusted according to the FY/MY conditions.

3.4 Scatterometer ice detection

Using the scatterometer characteristics, the anisotropy *anisFB* and the change of backscatter with incidence angle *dsigma* described in Section 2.2, the OSI SAF ice detection from scatterometer data was first derived using data from ERS Active Microwave Instrument (AMI) scatterometer [Breivik et al., 2001]. The algorithm was later redefined introducing a new parameter combining the properties of both the anisotropy and the dependency on the incidence angle [Breivik et al., 2012]. Having to deal with only one parameter we are also

ensuring that no mutually dependencies exist between parameters entering Eq. 3.2. To define the new parameter we use the three dimensional space of *differences between the three* σ_0 *measurements*. The three axis are defined as:

$$\begin{aligned} anisMF &= (\sigma_{0,mid} - \sigma_{0,fore}) / (\sigma_{0,mid} + \sigma_{0,fore}) \\ anisMB &= (\sigma_{0,mid} - \sigma_{0,back}) / (\sigma_{0,mid} + \sigma_{0,back}) \\ anisFB &= (\sigma_{0,fore} - \sigma_{0,back}) / (\sigma_{0,fore} + \sigma_{0,back}) \end{aligned} \quad (3.3)$$

The capital letters *F*, *M* and *B* refer to *mid*, *fore* and *back*, respectively. Closed sea ice has very low variations in anisotropy, and measurements over closed ice will therefore cluster around one point in the three dimensional space defined by Eq. 3.3. This *ice tie-point* can be used to represent closed ice. Measurements over open water will be scattered further away from the ice tie point. We then define the new parameter, *anisFMB*, to enter Eq. 3.2 as the *distance to this ice tie-point*. It is given by:

$$\begin{aligned} anisFMB^2 &= (anisMF - \overline{anisMF_{ice}})^2 + (anisMB - \overline{anisMB_{ice}})^2 \\ &+ (anisFB - \overline{anisFB_{ice}})^2 \end{aligned} \quad (3.4)$$

Whereas the classification of the sea ice edge makes use of *anisFMB*, the backscatter average is used for the sea ice type classification. Due to the backscatters dependency on incidence angle only the *fore* and *back* antenna data are used:

$$bscatt = \frac{1}{2}(\sigma_{0,fore} + \sigma_{0,back}) \quad (3.5)$$

Figure 5 shows parameters derived from one day of ASCAT scatterometer data over Arctic Atlantic on 15. January 2012. The upper panel of Figure 5 shows backscatter, which has been corrected for its dependency to the incidence angle. In parts of the area the limit between ice and open water is readily seen, however in large parts it is not, illustrating the difficulties in using the measured backscatter directly for ice edge detection. The two next panels shows the anisotropy coefficient, *anisFB*, and change of backscatter with incident angle, *dsigma*. The lowest panel shows the distance to the ice tie-point parameter, *anisFMB*, based on one day of ASCAT data. It gives a consistent and less noisy image of the ice edge compared to *anisFB* and *dsigma* used alone.

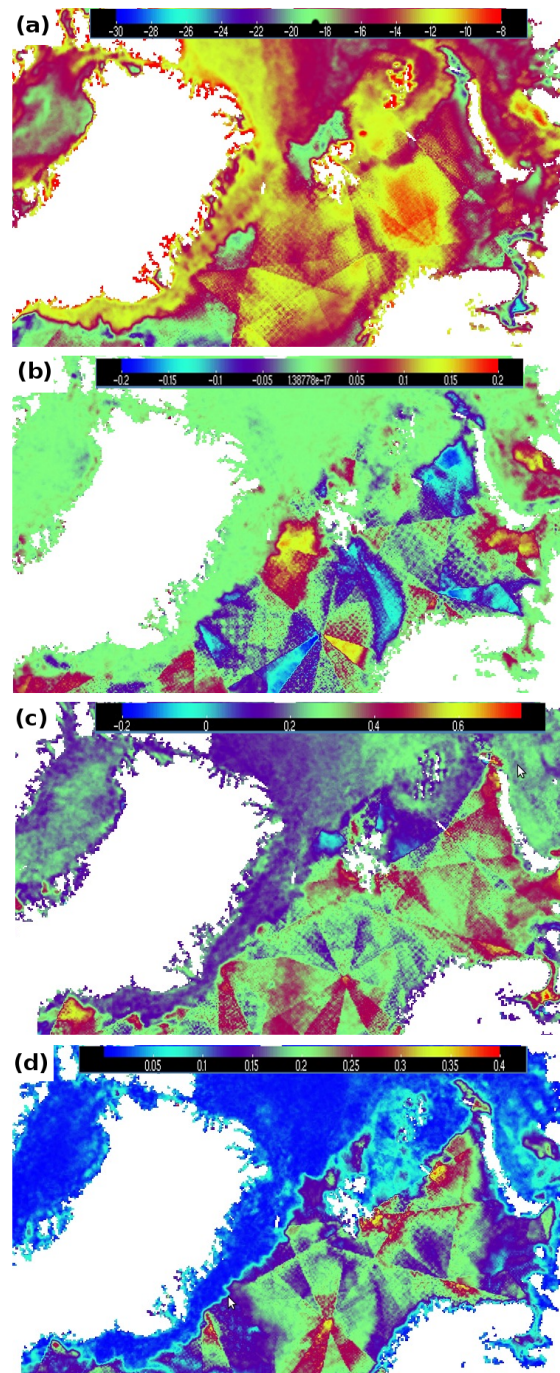


Figure 5: Parameters derived from one day of ASCAT scatterometer data (Metop-A) over Arctic Atlantic the 15th of January 2012. (a) Corrected backscatter (σ_0). (b) Anisotropy coefficient, *anisFB*. (c) Change of backscatter with incident angle, *dsigma*. (d) Distance to ice tie point, *anisFMB*.

Figure 6 shows mean value and standard deviation of *anisFMB* versus cell number for closed ice, open ice and open water classes based on the data from the Arctic, March and July 2007. Cell number 1 represents the outermost part of the swath, on both the left and right swath sections, i.e. both sides of the satellite ground track. The incidence angle decreases with increasing cell number. Table 4 shows the corresponding mean values and standard deviations of *anisFMB* for 5 different cell numbers across the ASCAT swath. From Figures 6 and Table 4 it is seen that the discrimination capability between water and closed ice is very good and stable for all cell numbers across the swath with slightly better discrimination capability in the winter season (March) than in summer (July). The discrimination capability between water and open ice is also good, however with a bit reduced discrimination capability in the summer season, when sea ice is melting and large melt ponds might occur on the ice surface. The discrimination utility between closed ice and open ice is less obvious.

To apply the Bayes method, we need knowledge of the shape of the probability distribution. We assume a normal distribution for all classes and use a Gaussian probability distribution function in Eq. 3.2. In Figure 7 is shown the distributions of *anisFMB* for the three ice edge classes, closed ice, open ice and open water, and *bscatt* for the two ice type classes, FY and MY, based on collocated data from December 2015 for cell number 20. We see that a Gaussian approximation holds good for both the FY, MY and the open water class. But for open ice and closed ice an asymmetric distribution (e.g. a Gamma distribution) would have been more correct. However, for simplicity we have chosen to rely on the Gaussian assumption which is reasonable based on qualitative judgement of the scatterometer density distributions in Figure 7 and also for PMW distributions in Figure 9. A quantitative estimation on how much uncertainty the use of Gaussian distribution really adds has not been thoroughly investigated. We will not claim this method alone as a very reliable tool for distinguishing between open and closed drift ice. The backscatter measurements are not linearly sensitive to variations of sea ice concentration and for good reasons scatterometer based ice concentration algorithms do not exist. However, including the open ice data in the training data set and in the classification gives higher sensitivity to variations in the marginal ice zone and the border between open water and ice.

Cell nr	Mean water	Std water	Mean open ice	Std open ice	Mean closed ice	Std closed ice
1	0.111	0.041	0.031	0.022	0.014	0.010
10	0.115	0.044	0.035	0.025	0.016	0.011
20	0.125	0.048	0.035	0.026	0.014	0.011
30	0.141	0.060	0.042	0.030	0.016	0.014
40	0.213	0.081	0.070	0.055	0.023	0.017

Table 4: Mean values and standard deviations of the parameter *anisFMB*, for 5 different cell numbers across the ASCAT scatterometer swath (Metop-A) valid for Arctic, March.

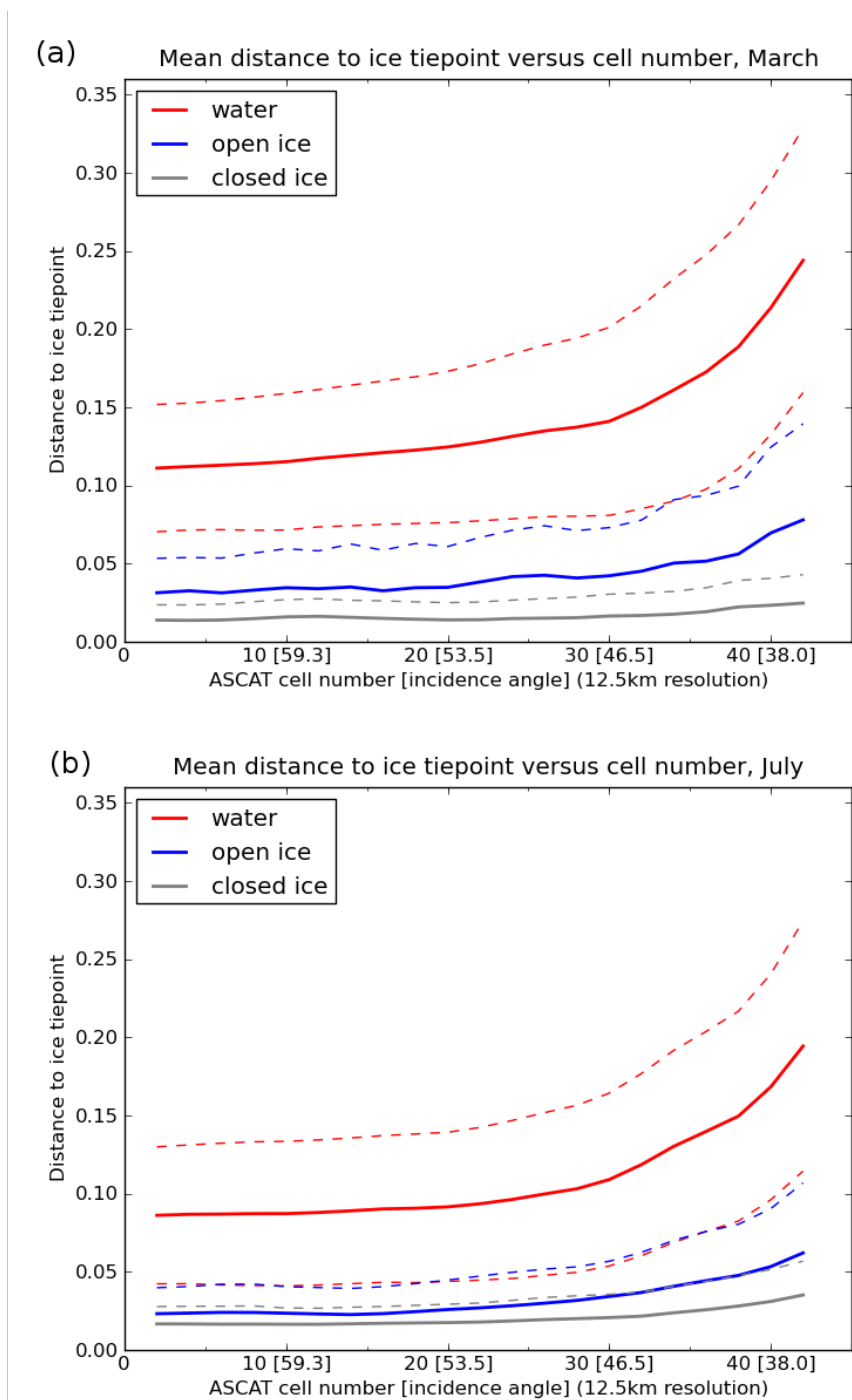


Figure 6: Mean values (solid lines) and standard deviation (dashed lines) of the parameter, anisFMB, for different ice classes as a function of cell number. Cell number one represents the outer part of the swath and the incidence angle decrease with increasing cell number. Northern Hemisphere, March 2007 (upper), July 2007 (lower).

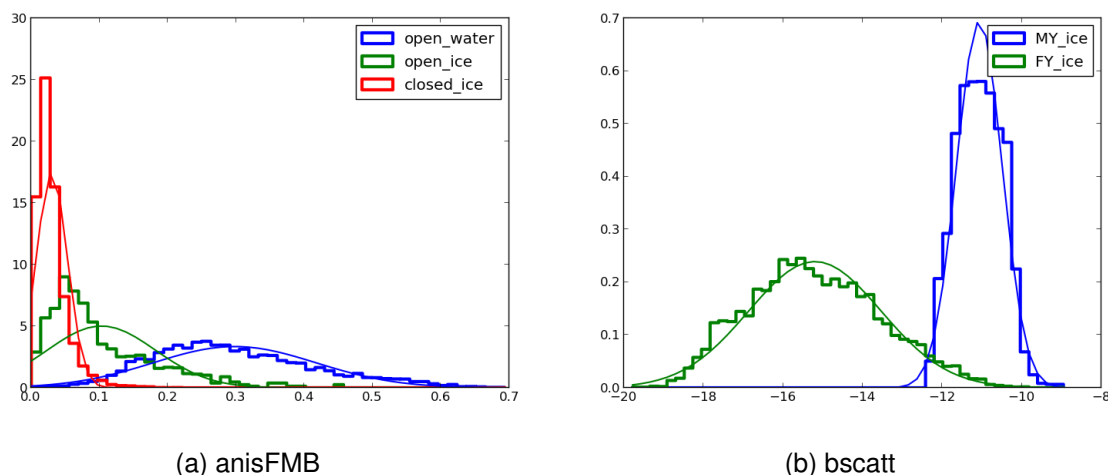


Figure 7: Density plot for the ascatt parameters: (a) *anisFMB* for sea ice edge classes closed ice (red), open ice (green) and open water (blue) and (b) *bscatt* for sea ice type classes first-year ice (green) and multi-year ice (blue). Data are collocated from Metop-B for cell number 20, December 2015. The stair plots show the data and the thin lines show the corresponding Gaussian fit to the data.

An example of ice edge analysis using ASCAT is given in Figure 8 and 10. In Figure 8 ASCAT analysis are compared to an AVHRR colour composite image, as well as to an analysis based on SSM/I data. The use of ASCAT reveals details in the ice edge not observed with use of the coarser resolution SSM/I data, as will be discussed in the next section.

Figure 10(a, b) shows the ASCAT analysis compared to a high resolution SAR wide swath image (150 m resolution) and it shows a good agreement between the ASCAT analysis and the ice extent observed in the SAR image. Figure 10(c, d) shows results using SSM/I data and is further discussed in the next section. Monitoring the results throughout a year has shown us that the ASCAT ice edge analysis are generally good and very often shows details in the ice edge in good agreement with high resolution satellite images. However, wind induced noise is also frequently observed. Since the analysis method relies on the interpretation of sea ice as an isotropic surface compared to the anisotropic surface created by a large scale wind field over open sea, problems with false ice detection sporadically arise when the open water sea surface seems isotropic because of a main wind direction parallel to the satellite ground track [see e.g. Breivik and Schyberg, 1998]. A way around this problem is to combine the ASCAT data with data from other satellites. The Bayesian approach offers an efficient framework for multi-sensor classification here combining ASCAT and PMW observations.

3.5 PMW ice detection

From PMW data three parameters are used in the OSI SAF multi-sensor approach. These are (see definitions in Eq. 2.1):

1. The polarization ratio in the 19 GHz channel, *PR19*

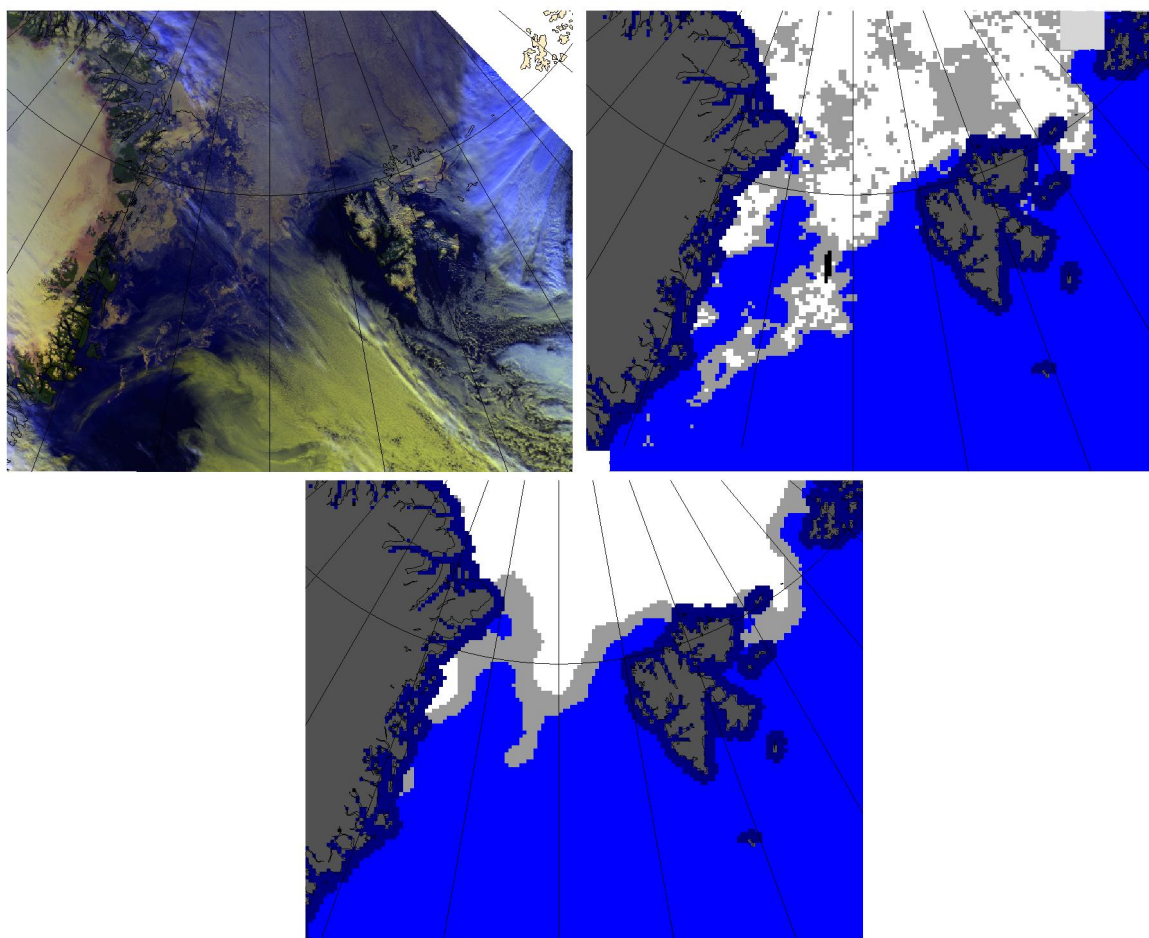


Figure 8: Sea ice conditions in the Fram Strait and the Barents Sea on the 31th of August 2008. Upper left: AVHRR colour composite image. Upper right: ASCAT derived ice edge. Lower: SSM/I (*GR1937*) derived ice edge.

2. The polarization ratio in the near 90 GHz channel, *PRn90*
3. The spectral gradient ratio, *GR1937*

Here, the frequency names are just representative for the true frequencies seen in Table 1. So, for instance the polarization ratio termed *PRn90* covers both SSM/I 85 GHz, SSMIS 91 GHz and AMSR2 89 GHz. The parameters are derived from the PMW TB's corrected for atmospheric influence as described in Section 2.1.1. Thus, collecting statistics from training data as described above, the probabilities $p(A_n|I_k)$ needed in Eq. 3.2 are found.

Figure 9 shows density plot for the SSMIS parameters based on data collocated from December 2015. In general, there is a very clear distinction with almost no overlap both between FY and MY (Figure 9d) and between open water and closed ice (Figure 9a, b, c). The distinction between open ice and the two other classes are less clear but usable. The probability of the three different ice classes, *closed ice*, *open ice* and *open water* can then be calculated based on the measured parameters *PR19*, *GR1937* and *PRn90* individually or in combination using Eq. 3.2. An example is given in the lower panel in Figure 8 and in Figure 10(c) and (d). The method provides reliable ice edge detections however with various

details as well as noise.

In summary, the 19 and 37 GHz data gives a smooth and noise free discrimination between the classes. The N90 gives more details, but are more sensitive to atmospheric noise mainly from water vapor. This applies both for SSM/I, SSMIS and AMSR2. Similarly ASCAT gives many details, but is affected by noise caused by wind over the ocean. A main goal in the OSI SAF is to utilize the relatively higher resolution information in ASCAT and N90 measurements compared to the 19 and 37 GHz, however in addition to take advantage of the more noise free measurements in 19 and 37 GHz channels. To achieve this the data is combined in a *stepwise* multi-sensor approach.

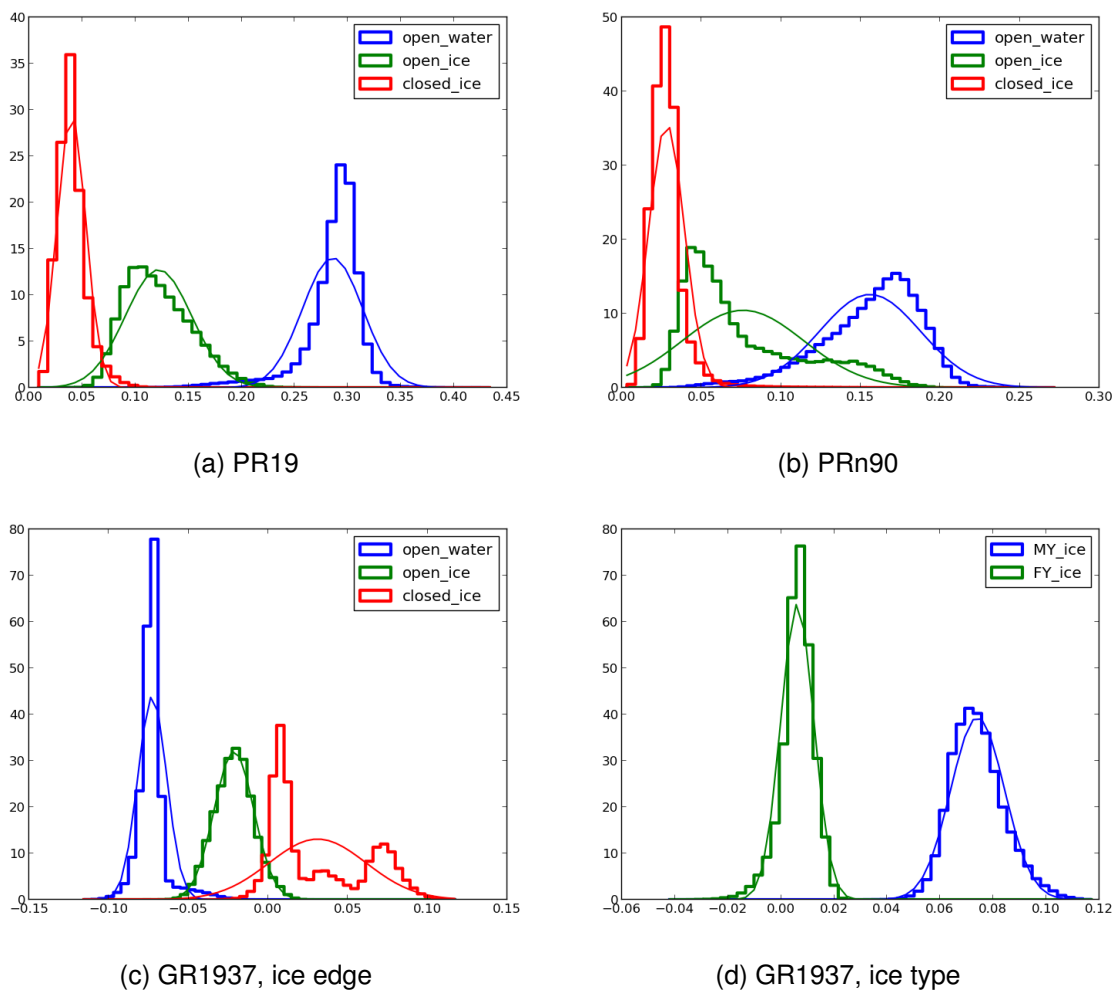


Figure 9: Density plot for the SSMIS parameters: (a) *PR19*, (b) *PRn90* and (c) *GR1937* for sea ice edge classes closed ice (red), open ice (green) and open water (blue), and (d) *GR1937* for sea ice type classes first-year ice (green) and multi-year ice (blue). Data are collocated from F18, December 2015. The stair plots show the data and the thin lines show the corresponding Gaussian fit to the data.

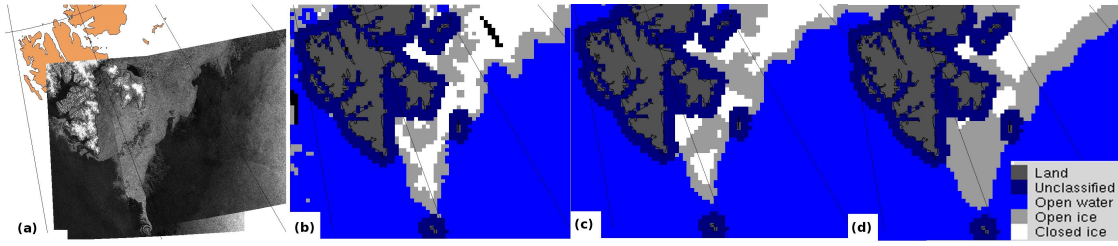


Figure 10: Sea ice south of Svalbard 30 January 2009. (a) A Radasat-2 image, (b) analysis based on ASCAT (*anisFMB*), (c) SSM/I *PRn90*, (d) SSM/I combined *PR19* and *GR1937*.

3.6 Multi-sensor ice edge analysis, OSI-402-c

The OSI SAF ice edge product is using the three PMW parameters, *PR19*, *GR1937* and *PRn90* and the ASCAT parameter *anisFMB*. In **the first step** ice class-probabilities are estimated on the satellite swath projection for each passage. A direct application of Eq. 3.2 on all of the four parameters gives a result dominated by the lower resolution data from *PR19* and *GR1937* where details in the ice edge are smoothed away. Instead, the probabilities are in this first step estimated for the lower resolution and the higher resolution individually. Eq. 3.2 is used to get the following three estimates on the ice probabilities on swath data:

- $p(I_k | PR19, GR1937)$ which combines the two low-resolution parameters
- $p(I_k | PRn90)$ and
- $p(I_k | anisFMB)$

where I_k represents the k ice classes: closed ice, open ice and water. These probability estimates are carried out for each instrument- and satellite specific data set and use the corresponding dynamical PDF's. Note, that hereafter the combination of parameter *PR19* and *GR1937* is called *PMW19/37*.

While computing probabilities is best performed in swath projection (e.g. because of the angular dependency of the PDF's for the ASCAT instrument), the step of multi-sensor analysis must be performed on gridded, daily composited probabilities, in order to achieve collocation of the several satellite platforms. So, in **the second step** the ice class probabilities for each of the three estimates above are gridded onto the OSI SAF grid based on one day of swath-data. Here, probability estimates from both Metop-A and Metop-B are combined into one gridded product. The OSI SAF grid is a polar-stereographic grid with 10 km spatial resolution. The gridding is performed using a simple analysis method where each satellite observation is influencing the grid points within its *influence radius* (R_i) which is scaled to the measurement footprint size (see Table 1). Table 5 summarizes the influence radius for each instrument. Observations are given weight dependent on the distance D from the observation center to the grid-point. i.e. observations nearest the grid point carry the most weight. As the distance increases, the observations carry less weight, and outside R_i the satellite observation has no influence. The weighting function W is given in Equation 3.6.

$$W = \begin{cases} 1 - \frac{D}{R_i} \cdot 0.3 & \text{for } D < R_i, \\ 0 & \text{for } D \geq R_i \end{cases} \quad (3.6)$$

Sensor	Platform	Parameter	Influence radius [km]
SSMIS (SSM/I)	F18	PMW19/37	18
		N90	9
ASCAT	Metop-A/ Metop-B	anisFMB	10
		bscatt	10
AMSR2	GCOM-W1	PMW19/37	10
		N90	5

Table 5: Influence radius used for the different sensors and parameters in the daily gridding of swath data.

The result is that for each of the three ice edge classes we get: two daily gridded probability products for SSMIS, one product for ASCAT, and two products for the new AMSR2 data. At this point, the gridded fields (PMW19/37 and N90) from SSMIS and AMSR2 are combined into optimized gridded PMW fields that will be used in the multi-sensor calculations. At present the AMSR2 data are prioritized over SSMIS data due to the better sampling resolution. This means, that as default the PMW input to the multi-sensor is based on AMSR2 data only. However, any missing AMSR2 grid data or gaps due to *Gross Error*² data, are filled with SSMIS grid data to archive the best possible PMW daily grids at any time to be used as input to the multi-sensor calculations.

Figure 10 is an example from January 2009, showing the three analyzes based on anisFMB, PRn90 and PMW19/37, respectively, and compared to a Radarsat-2 wide swath image. The resolution, or footprint diameter, of the PMW19/37 measurements is approximately 50 km, while for PRn90 it is approximately 15 km. As the analysis is performed on a 10 km grid we would like to keep the higher resolution information provided by PRn90. However, PRn90 is much more affected by atmospheric noise than PMW19/37. The ASCAT input data is provided on a 12.5 km grid, with a resolution of 25-30 km and by that providing also better resolution than PMW19/37. But the ASCAT data is also noisy and the uncertainty of the measurements is relatively higher than for PMW19/37. To utilize more of the smaller scale information in ASCAT and PRn90, the final step introduce a approach where $p(I_k|PRn90)$ and $p(I_k|anisFMB)$ are combined in a multi-sensor approach and $p(I_k|PR19, GR1937)$ is instead used as a filter. So, **the final step** in the multi-sensor analysis is carried out in two steps:

1. The daily ice class probabilities on the grid is estimated from the gridded probabilities based on PRn90 and anisFMB by using a form of Eq. 3.2.
2. The probabilities based on PMW19/37 are then used as a filter where:
 - A grid point where $p(water|PMW19/37)$ exceed 50 % is classified as water.
 - A grid point where $p(closed\ ice|PMW19/37)$ exceed 50 % is classified as closed ice.
 - A grid point without PMW19/37 data is not processed but classified as "no data".

The resulting analysis gives a sharper ice edge with more details and with limited spurious

²By Gross Error is meant data that for some reason are non-physical and out of reasonable range of value.

ice.

An example is given in Figure 11. The figure shows the ice edge analysis based individually on (b) anisFMB, (c) PRn90, (d) PMW19/37. The lower right panel (e) shows the multi-sensor analysis using PMW19/37 as a filter. For reference, a NOAA-17 AVHRR image on the same date is also shown at the left panel (a).

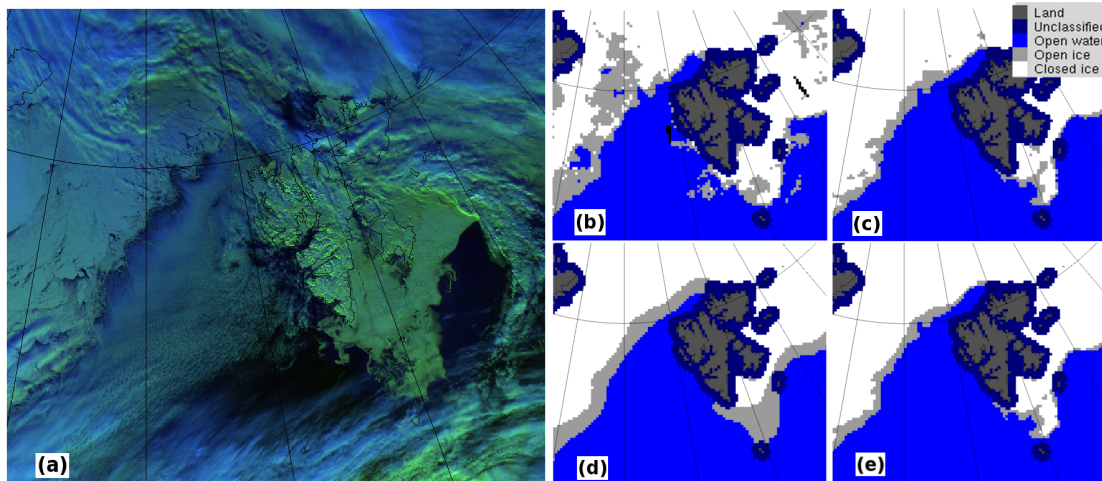


Figure 11: Sea ice around of Svalbard March 29, 2009. (a) A Metop AVHRR image, (b) analysis based on anisFMB, (c) PRn90 and (d) PMW19/37. (e) is showing the multi-sensor analysis using PMW19/37 as a filter.

3.7 Multi-sensor ice type analysis, OSI-403-c

The multi-sensor method is also used to discriminate between FY and MY sea ice. Due to increased internal scattering in MY the change in TB as a function of frequency can be used to distinguish between ice types [Steffen et al., 1992]. For PMW data the spectral gradient ratio of the 19 and 37 GHz, $GR1937$, is therefore a good parameter to use in ice type classification. For scatterometer the backscatter from the sea ice surface is dependent on ice age. The larger backscatter over MY than FY makes the ASCAT average backscatter, ($bscatt$ in Eq 3.5), useful for ice type classification. More details and examples are given in the ASCAT algorithm development report of Breivik and Eastwood [2009].

Using these two parameters the probabilities of ice type is calculated in a similar manner as for ice edge:

1. For each of the two parameters, $GR1937$ and $bscatt$, successive estimation of ice type probability is carried out on the satellite swath data.
2. Each parameter estimation of ice type probability is gridded onto the OSI SAF grid based on one day of data input. Again, ASCAT data from Metop-A and Metop-B is combined into one.
3. As for ice edge the PMW input to the multi-sensor analysis is a combination of SSMIS and AMSR2 in the way that AMSR2 data is prioritized whenever AMSR2 grid data are

available, and replaced/filled with SSMIS data whenever AMSR2 data are missing.

4. Finally the daily multi-sensor analysis is carried out on the OSI SAF grid with the gridded probability fields as input.

In the final step, the results from the ice edge analysis are used to classify open water and hereby remove noise over open water.

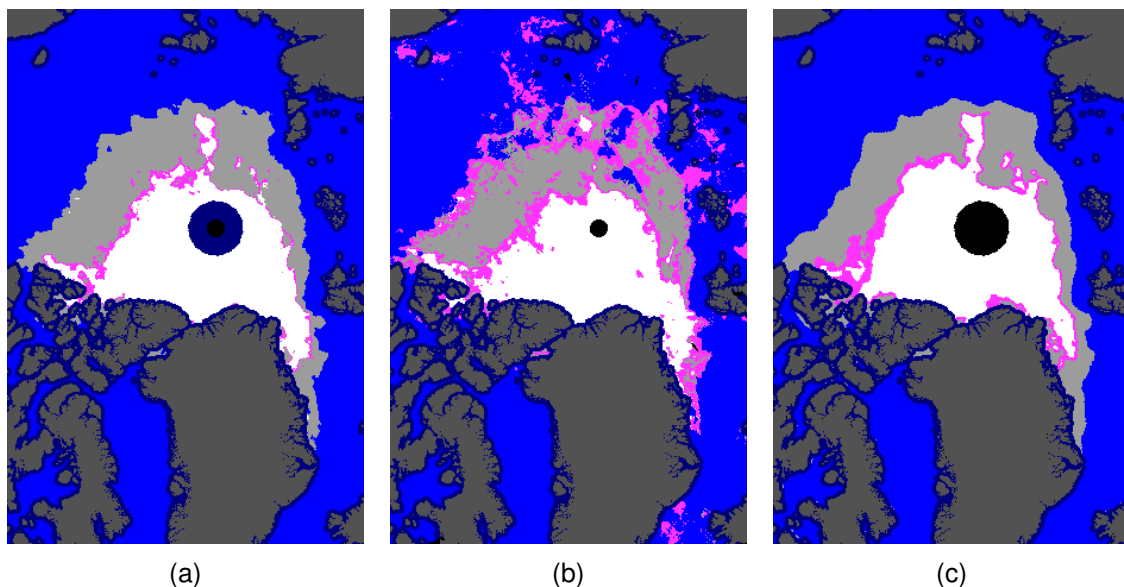


Figure 12: OSI SAF sea ice type (2012-10-02) showing MY (white), FY (gray), open water (blue) and ambiguous (pink). (a) Multi-sensor product, (b) Product from only ASCAT backscatter, and (c) Product from only SSM/I GR1937.

Figure 12 shows an example of the ice type analysis in the Arctic. The two figures to the right represent *step 2*, that is, the analysis based individually on ASCAT backscatter and GR1937, respectively. The figure to the left represents the final multi-sensor analysis (*step 3*). The multi-sensor analysis shows to be able to preserve details from the high resolution ASCAT while avoiding large part of its noise.

In summer, when the FY gradually decreases or becomes multi-year ice, the distinction between ice types becomes very difficult. This is partly due to melting resulting in wet ice and water on the ice. As a result, in the summer season basically from May to October there is no information on ice type in the data and the ice type is classified as "uncertain" in this period.

4. Preliminary Validation and Technical Issues

4.1 Preliminary validation results

The OSI SAF algorithm for sea ice edge and type has been running in a test period with the inclusion of ASCAT data from Metop-B, SSMIS data from F18 and AMSR2 data. In the following sections the performance of the new instruments from the test period is presented.

4.1.1 Time series of PDF's from new satellites versus operational ones

Calculations of the dynamical PDF's based on the new instruments are shown in the figures below in order to see how they eventually differ from instruments in the operational algorithm.

Figure 13 shows the PDF's based on Metop-B and Metop-A, respectively, back to 2015-10-01. The general trend is that they compare well within this period and at the same time they behave in a comparable way as the five years reprocessed data seen in Appendix A (Figures A.4 and A.6).

Figures 14–17 compare the PDF's based on the three PMW instruments, SSMIS-F17, SSMIS-F18 and AMSR2-GW1, for the different parameters used in the analysis: *PR19*, *PRn90*, and *GR1937* for both edge and type. In general, the PDF's from F18 compare well with the PDF's from F17 and again they compare well with the reprocessed data in the appendix (Figures A.1–A.3 and A.5).

In the PDF's from AMSR2 there seem to be some smaller differences relative to the SSMIS, such as for instance slightly higher values of the AMSR2 PDF's for (*open water*, *PR19*) and (*open water*, *PRn90*), and a larger standard deviation for AMSR2 PDF's (*open ice*, *PR19*). This may be a result of the slightly different frequencies (Table 1). Despite these smaller differences, the AMSR2 PDF's show same behavior as the SSMIS PDF's.

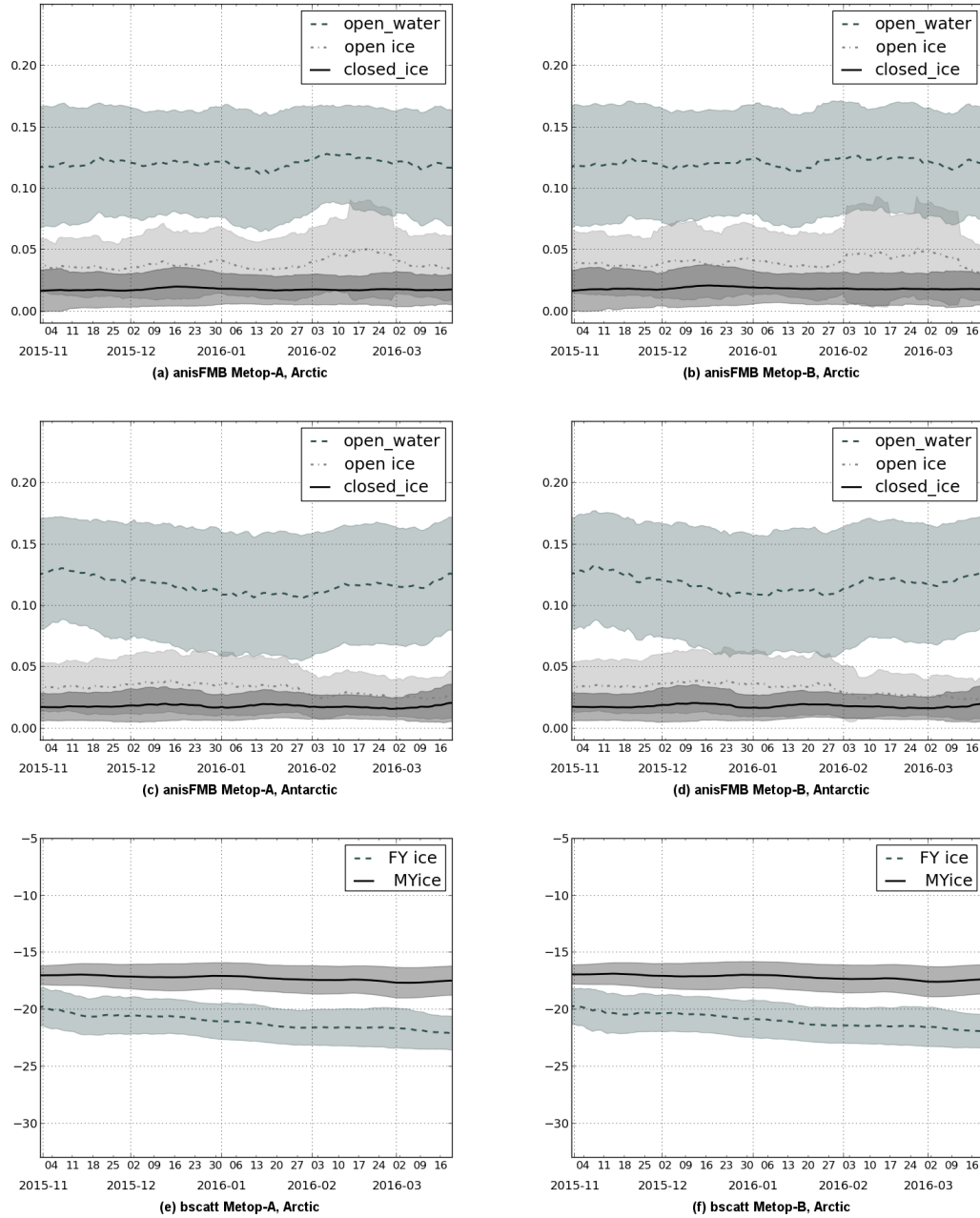


Figure 13: Dynamical PDF's (mean \pm std) of the ASCAT parameters from Metop-A (left column) and Metop-B (right column), respectively. (a) – (b) show *anisFMB* for the ice edge classes, Northern Hemisphere. (c) – (d) show *anisFMB* for sea ice edge classes, Southern Hemisphere. (e) – (f) show *bscatt* for sea ice type classes, Northern Hemisphere. The daily PDF's for FY are absent until the 10th of October due to too little FY ice in late summer.

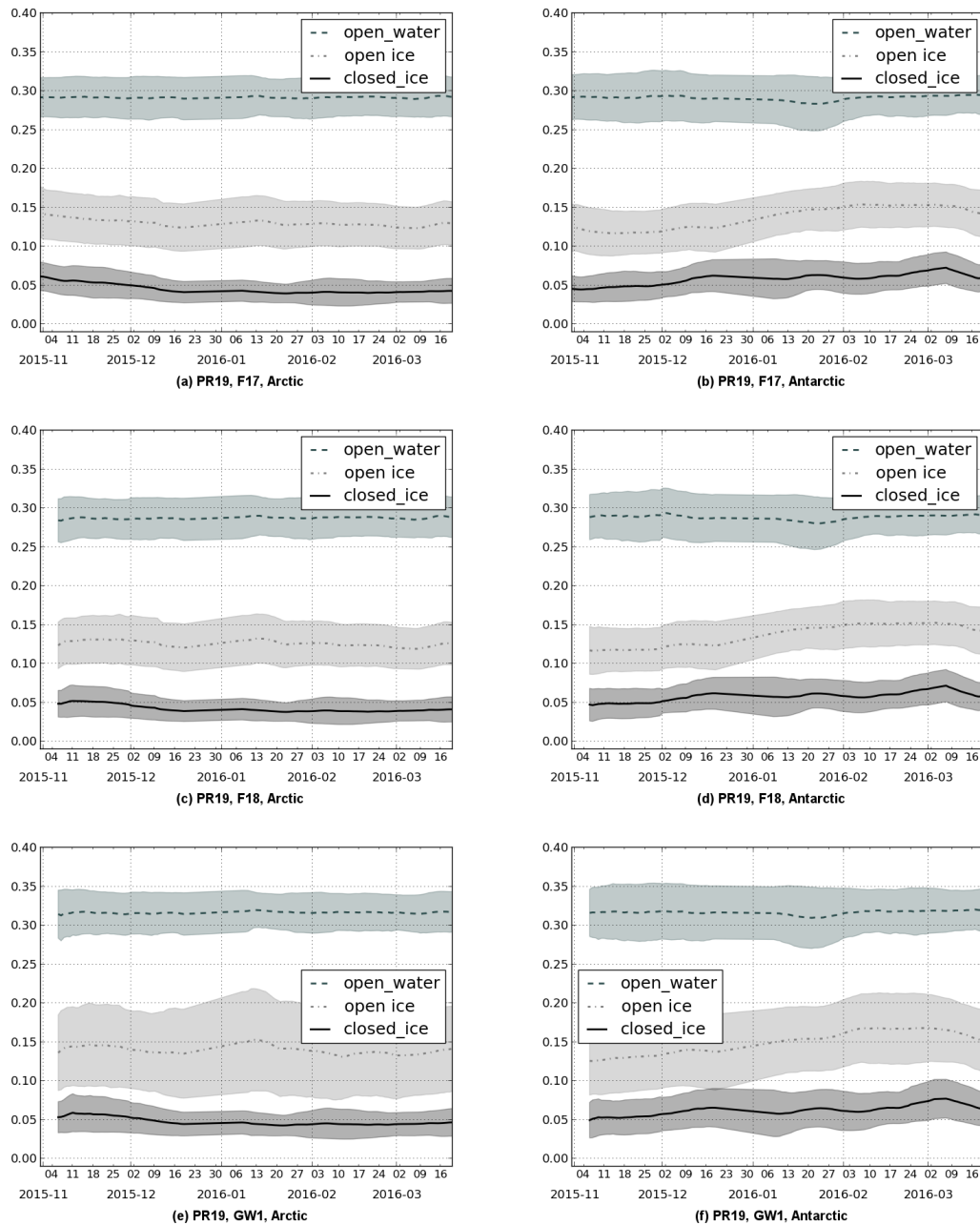


Figure 14: Dynamical PDF's (mean \pm std) of the PMW parameter $PR19$ for sea ice edge classes for the Northern Hemisphere (left column) and Southern Hemisphere (right column). (a) – (b) show SSMIS data from F17. (c) – (d) show SSMIS from F18. (e) – (f) show AMSR2 data from GW1.

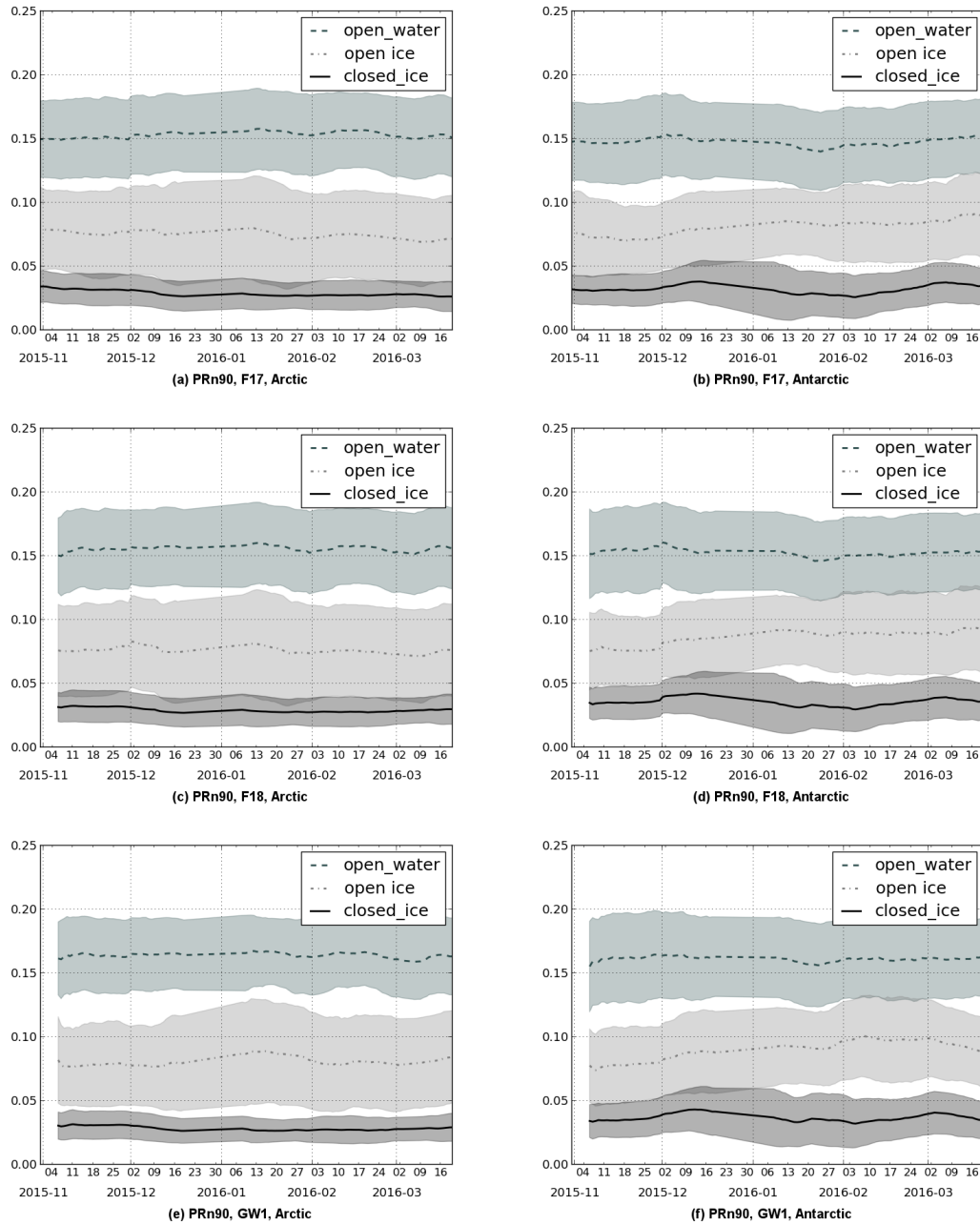


Figure 15: Dynamical PDF's (mean \pm std) of the PMW parameter $PRn90$ for sea ice edge classes for the Northern Hemisphere (left column) and Southern Hemisphere (right column). (a) – (b) show SSMIS data from F17. (c) – (d) show SSMIS from F18. (e) – (f) show AMSR2 data from GW1.

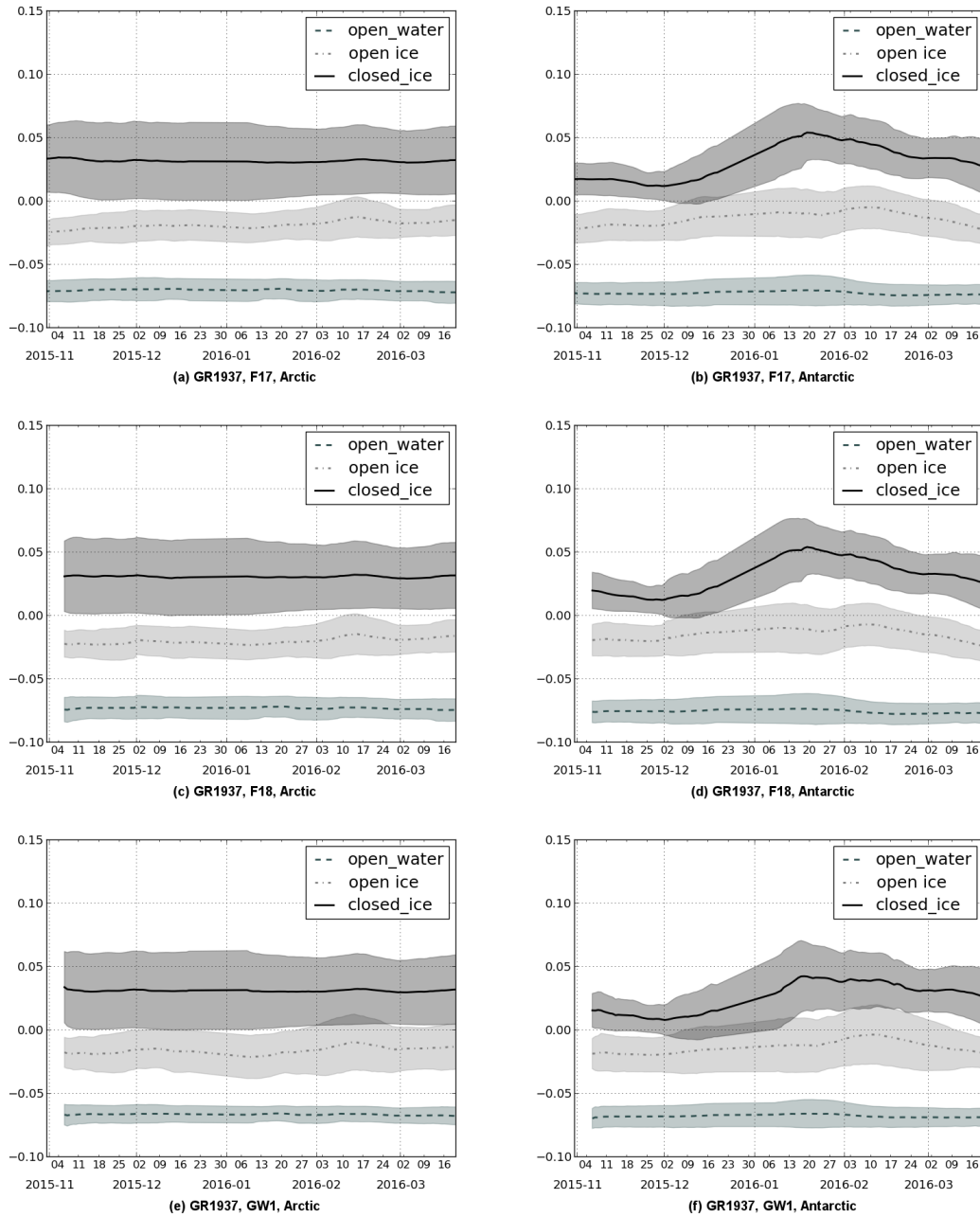


Figure 16: Dynamical PDF's (mean \pm std) of the PMW parameter *GR1937* for sea ice edge classes for the Northern Hemisphere (left column) and Southern Hemisphere (right column). (a) – (b) show SSMIS data from F17. (c) – (d) show SSMIS from F18. (e) – (f) show AMSR2 data from GW1.

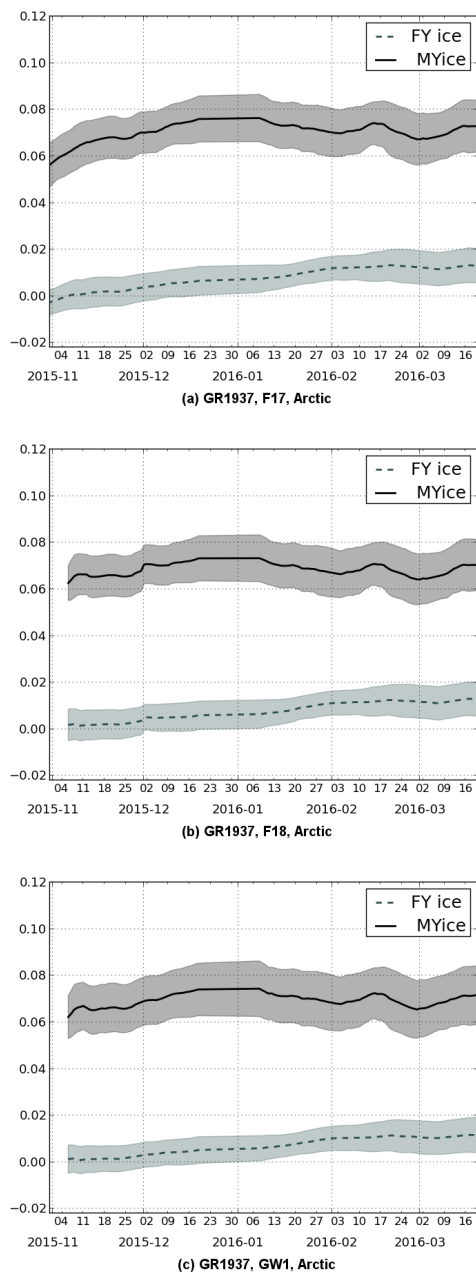


Figure 17: Dynamical PDF's (mean \pm std) of the PMW parameter $GR1937$ for sea ice type classes for the Northern Hemisphere. (a) shows SSMIS data from F17. (b) shows SSMIS from F18. (c) shows AMSR2 data from GW1.

4.1.2 Inclusion of ASCAT from Metop-B

The characteristics of ASCAT data from Metop-B are very similar to ASCAT data from Metop-A, and the continuation of the multi-sensor product including Metop-B will give no change in the product quality. In the period we have now with overlap of the two satellites the result of including data from both satellites is a significantly better coverage. This is more relevant for the Southern Hemisphere where the sea ice edge is found at lower latitudes than in the Northern Hemisphere. Figure 18 shows the data coverage - here given in terms of the probability of *closed ice* - on the 9th of December 2015 for Metop-A, Metop-B and both combined, respectively. Due to the displaced satellite path between Metop-A and Metop-B we see almost no missing data holes in the combined Metop data.

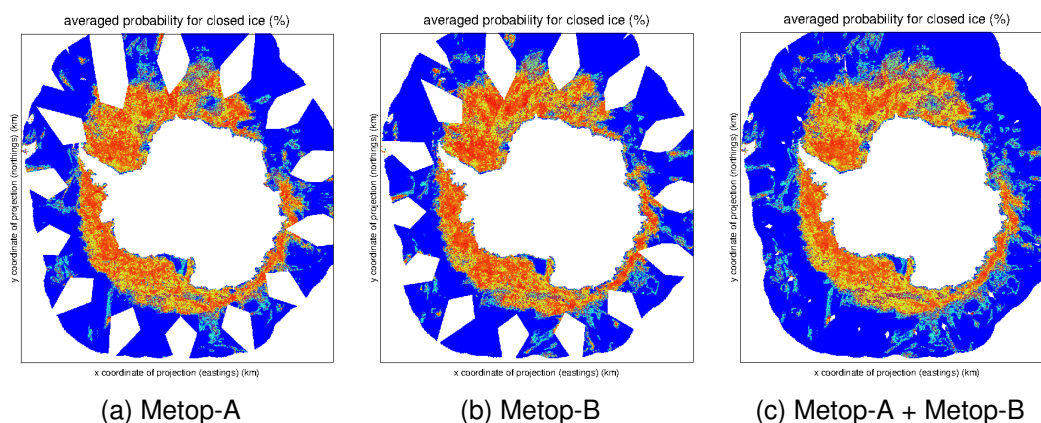


Figure 18: Swath coverage on the 9th of December 2015 on Southern Hemisphere, of ASCAT data from (a) Metop-A, (b) Metop-B and (c) Metop-A and Metop-B combined. Colors represent probabilities of *closed ice* where reddish is higher probability, blue is low probability and white is 'land or 'no data'.

4.1.3 Switch to SSMIS from F18

The characteristics of SSMIS data from F17 are very similar to SSMIS data from F18, and the continuation of the multi-sensor product including SSMIS F18 will give no change in the product quality.

4.1.4 Inclusion of AMSR2 data

The AMSR2 instrument have very similar behavior and similar channel properties as the SSMIS instrument (Section 4.1.1 and Table 1). The major difference is the higher spatial resolution and shorter sampling interval of the AMSR2. The spatial resolution of the lowest frequency, 18.7 GHz, is comparable with the SSMIS highest frequency of 91 GHz. This allows also for a smaller influence radius (Table 5) when carrying out the daily gridding of swath data and therefore will keep more details in the ice patterns.

During the test period (November-December, 2015), the sea ice edge and type algorithm has been run on two parallel runs:

- The *operational* multi-sensor analysis based on SSMIS and ASCAT,
- The *new* multi-sensor analysis based on AMSR2 and ASCAT.

In Figure 19 is shown single day examples of the ice edge and –type outcome from the two parallel runs for the Northern Hemisphere, and Figure 20 shows the ice edge outcome for the Southern Hemisphere. In general they seem to capture the same patterns, however with more details along the ice edges when including AMSR2.

In a Bayesian multi-sensor estimate not only the spatial resolution matters, but also the probability values which decide how much each measurement is weighted. As described in Section 3.6, the probabilities for each of the ice classes are estimated on daily gridded fields for each instrument. Figure 21 shows, in density distribution plots, the higher probabilities in the daily gridded field for each of the ice edge classes. For comparison values from the SSMIS based probabilities are shown together with the AMSR2 based probabilities. For all the three high frequency classes the AMSR2 turns out to be distributed slightly towards higher probabilities than SSMIS. For the PMW19/37 both SSMIS and AMSR2 have very high probabilities and few probabilities below 90%. This is also why PMW19/37 will dominate the multi-sensor estimates and therefore instead is used as a filter on the higher frequency output.

As a result of both the higher spatial resolution of AMSR2 and the tendency of higher ice class probabilities from AMSR2, the AMSR2 will be prioritized over SSMIS in the multi-sensor analysis. The PMW input to the Bayesian approach will consist of mainly AMSR2 data but will be replaced by SSMIS data whenever AMSR2 data are missing.

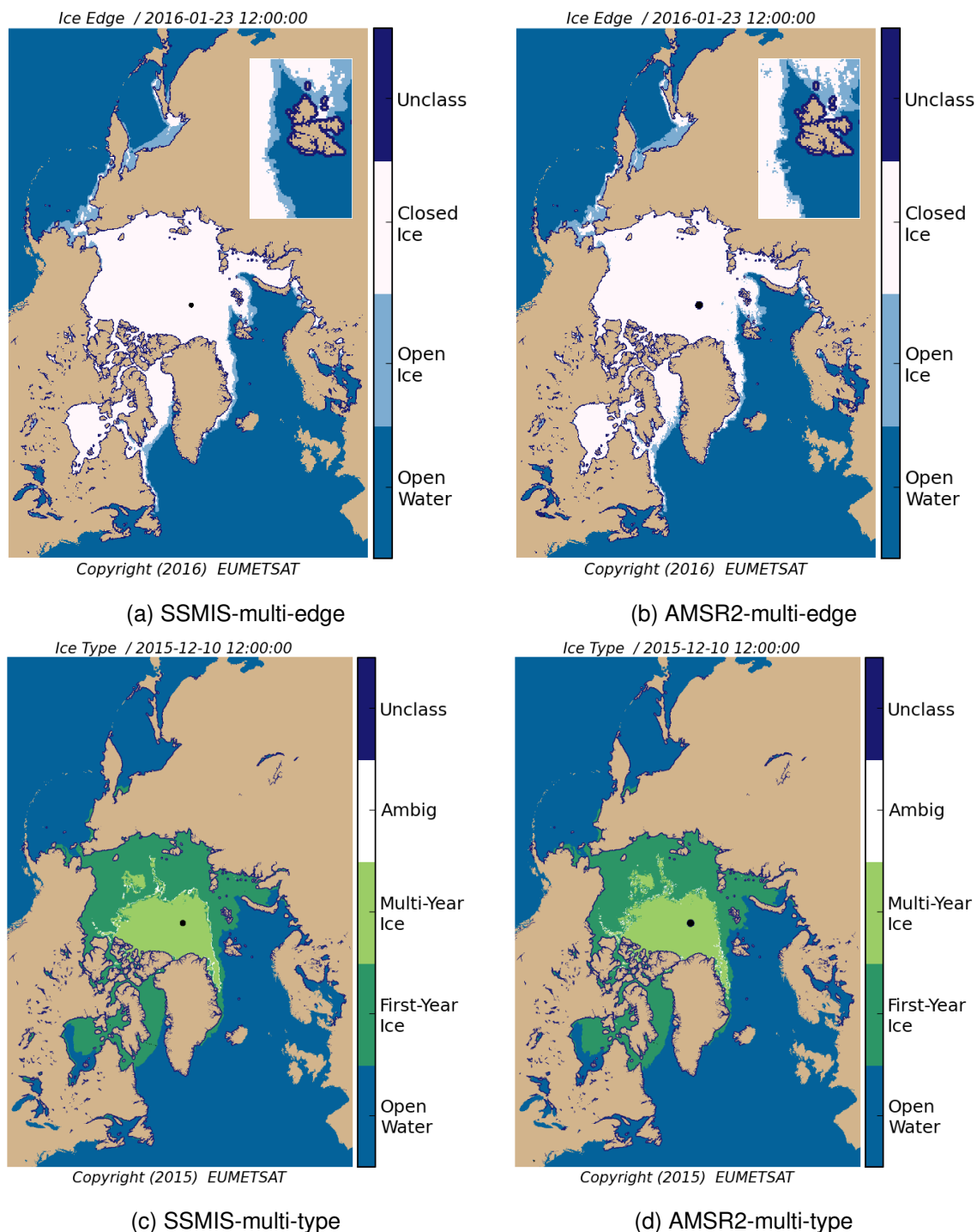


Figure 19: Comparison of the *operational* and *new* OSI SAF sea ice multi-sensor products for Northern Hemisphere: (a) Sea ice edge based on SSMIS & ASCAT (2016-01-23) with inset showing a zoom of the ice edge around Svalbard, (b) Sea ice edge based on AMSR2 & ASCAT (2016-01-23) with inset showing a zoom of the ice edge around Svalbard, (c) Sea ice type based on SSMIS & ASCAT (2015-12-10), (d) Sea ice type based on AMSR2 & ASCAT (2015-12-10).

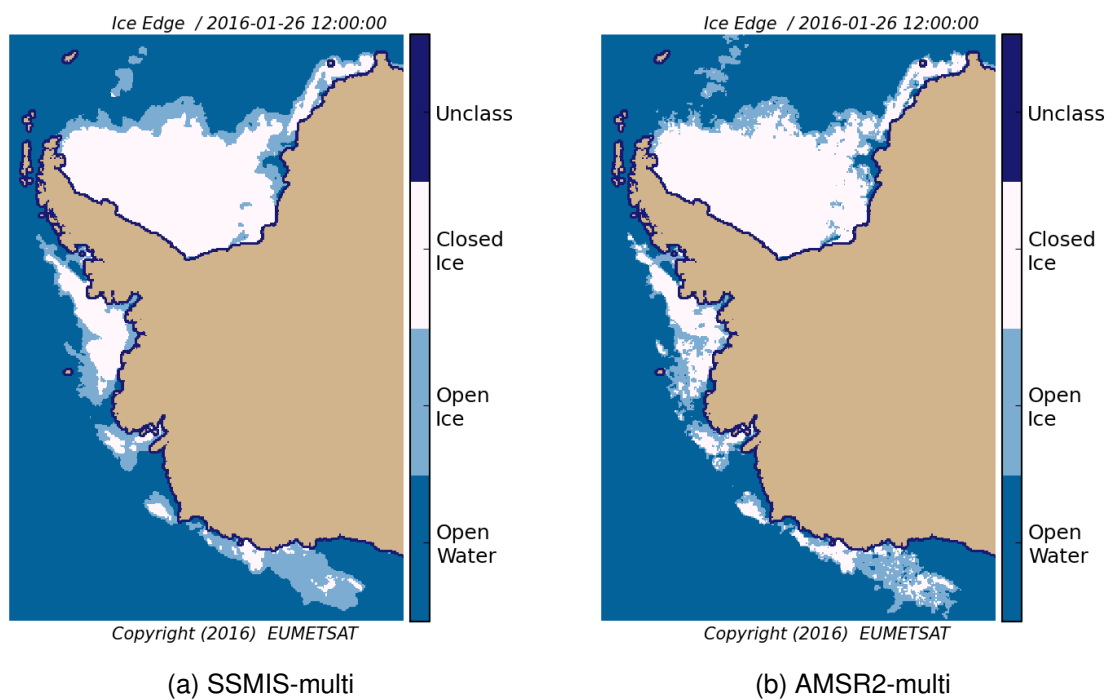


Figure 20: Comparison of the *operational* and *new* OSI SAF sea ice multi-sensor products (2016-01-26) for the Weddell Sea region in the Southern Hemisphere: (a) Sea ice edge based on SSMIS & ASCAT, (b) Sea ice edge based on AMSR2 & ASCAT.

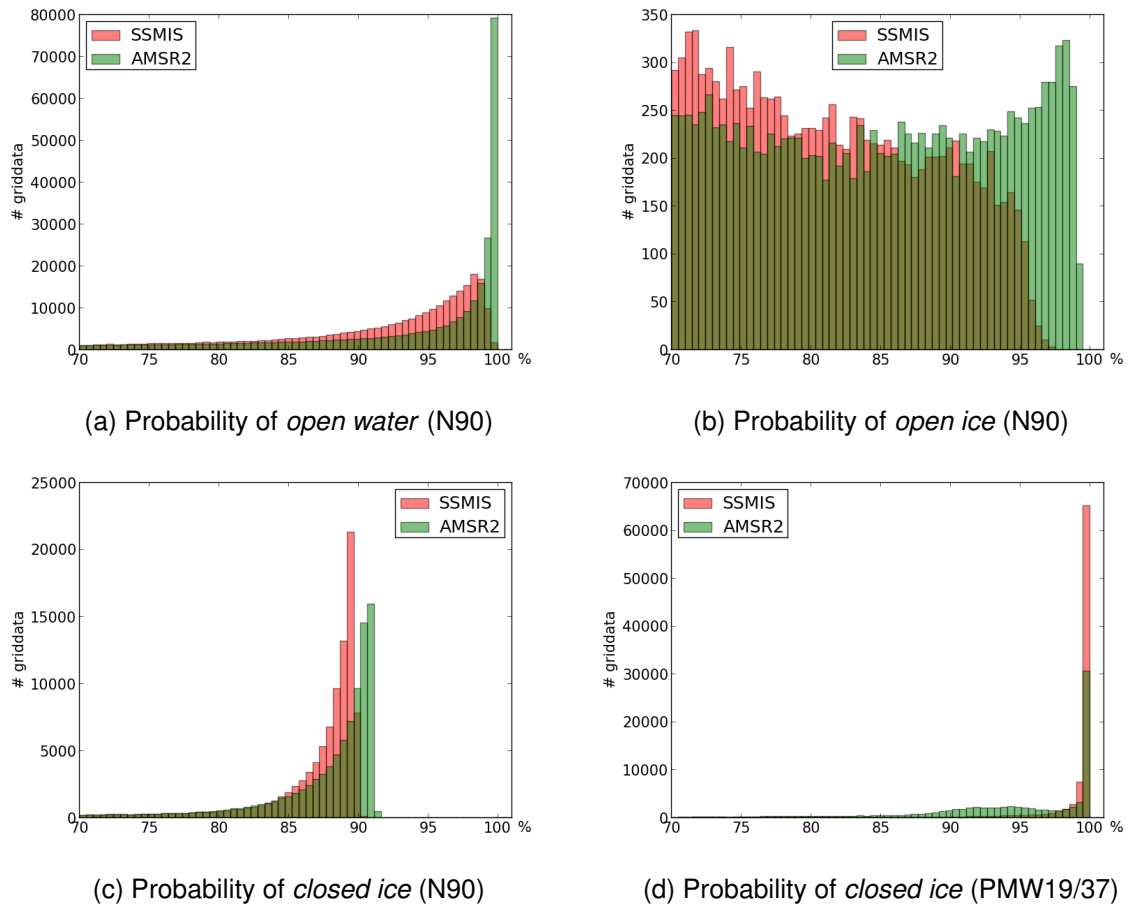


Figure 21: Density distribution plot of the daily gridded probabilities (02-12-2015, Northern Hemisphere) for comparison of the SSMIS (*red*) and AMSR-2 (*green*) performances: (a) Probability of *open water* for the near 90 GHz, (a) Probability of *open ice* for the near 90 GHz, (a) Probability of *closed ice* for the near 90 GHz, (a) Probability of *closed ice* for PMW19/37.

4.2 Exception handling

4.2.1 Missing input data

In the case of missing input data the result is flagged. For each point in the final multi sensor analysis grid where input data is missing, data data point is set to “Missing data”. In the case of no input data being available at all, the whole product will be set to “Missing data”, and still be delivered.

4.3 Assumptions and Limitations

4.3.1 Assumption on distribution type

As described in chapter 3.3 above we have assumed Gaussian probability density distributions for all ice classes. From Figure 7 and Figure 9 we see that this holds good for the open water class but not necessarily for the two ice classes. For open ice, and in particular closed ice, an asymmetric distribution would have been more correct. However, for simplicity we have chosen to use the Gaussian assumption.

4.3.2 Limitation on ice type product period

The sea ice type product will only contain classified data (*First-year Ice*, *Multi-year Ice*) in the period from mid-October to mid-May. From mid-May until mid-October all data over ice will be marked as “*ambiguous*”.

4.3.3 No ice type classification on Southern Hemisphere

The ice type product will only contain classified data in the Northern Hemisphere product area. The Southern Hemisphere product has no or very little multi-year sea ice, and the sea ice surface is quite different from the Northern Hemisphere. So, all data points with ice in the Southern Hemisphere is marked as “*ambiguous*”.

A. Time series of PDF's - dynamical versus static

The present algorithm, including dynamical PDF's, has been tested out by reprocessing data from 2010-2014. Below, the daily estimates of PDF is shown as the *mean value* \pm the *standard deviation* (STD). Each figure represent one of the satellite parameters. That is, *PR19*, *PR91* and *GR1937* are shown for the ice edge classes, and *GR1937* and *bscatt* are shown for the ice type classes. PDF's for Southern Hemisphere are represented for the year 2014 in Figure A.7. When the std-regions of the different classes are distinctively different (not overlapping), the algorithm should do well in the classification, whereas overlapping between the different PDF's causes uncertainties in the classification.

The very high std-values for static PDF's seen in Figures A.5f and A.6f are manually set to mark that the period is uncertain and sea ice type is classified as *ambiguous*.

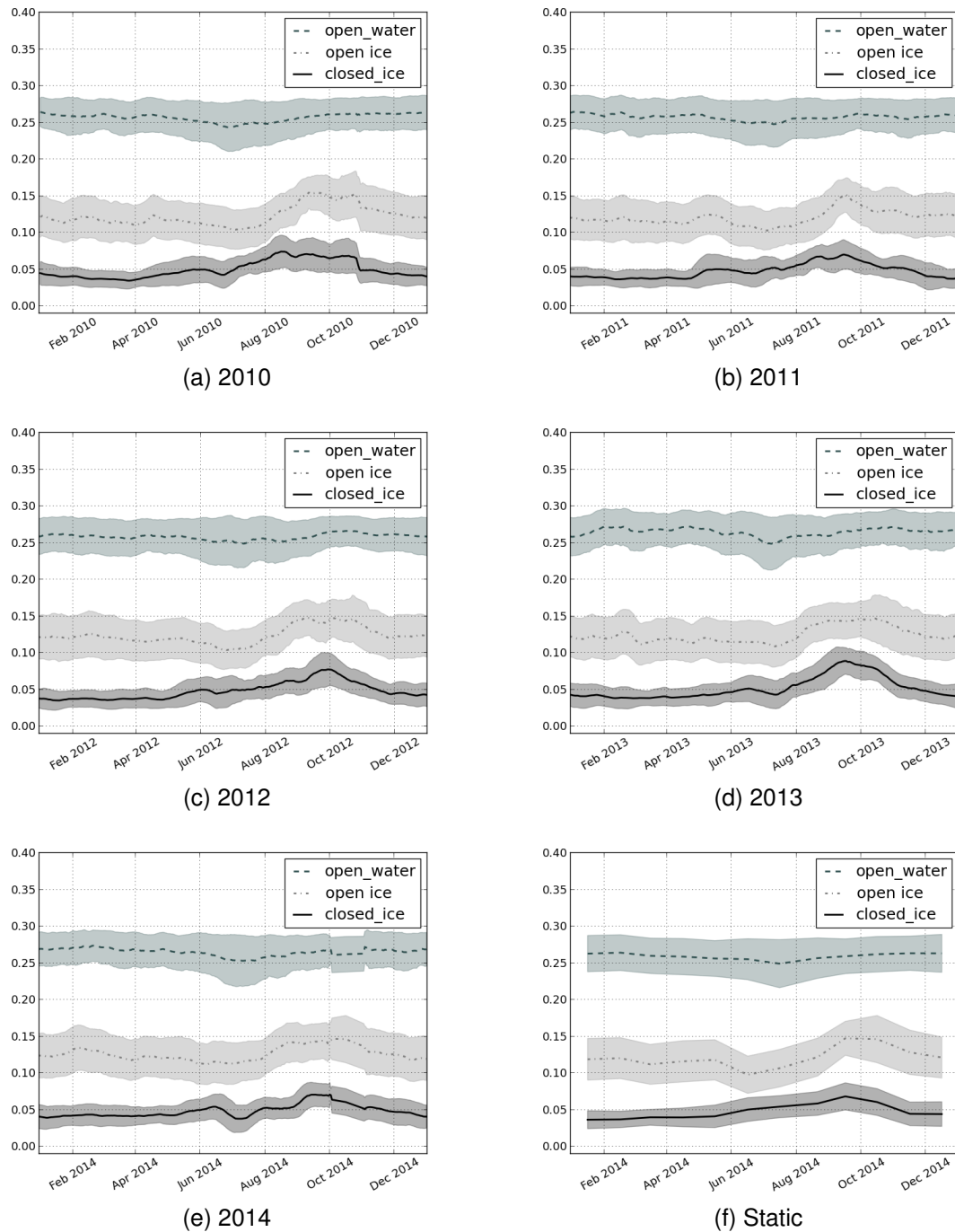


Figure A.1: Dynamical PDF's (mean \pm std) of the SSMIS parameter *PR19* for *open water*, *open ice*, and *closed ice*, respectively, for the Northern Hemisphere. Statistics are for the year (a) 2010, (b) 2011, (c) 2012, (d) 2013, and (e) 2014. (f) shows the corresponding static PDF's based on a year of data 2007-2008.

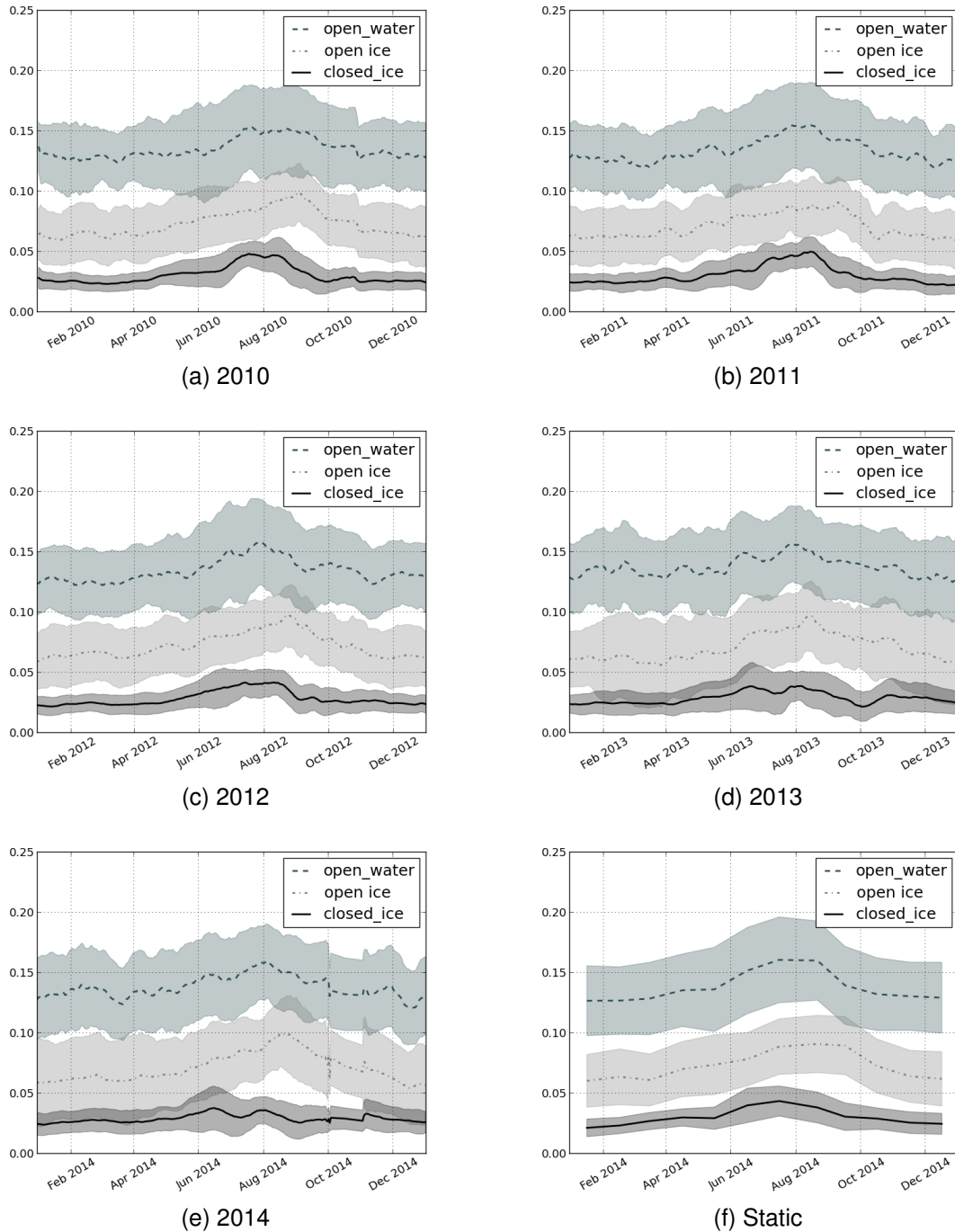


Figure A.2: Dynamical PDF's (mean \pm std) of the SSMIS parameter *PR91* for *open water*, *open ice*, and *closed ice*, respectively, for the Northern Hemisphere. Statistics are for the year (a) 2010, (b) 2011, (c) 2012, (d) 2013, and (e) 2014. (f) shows the corresponding static PDF's based on a year of data 2007-2008.

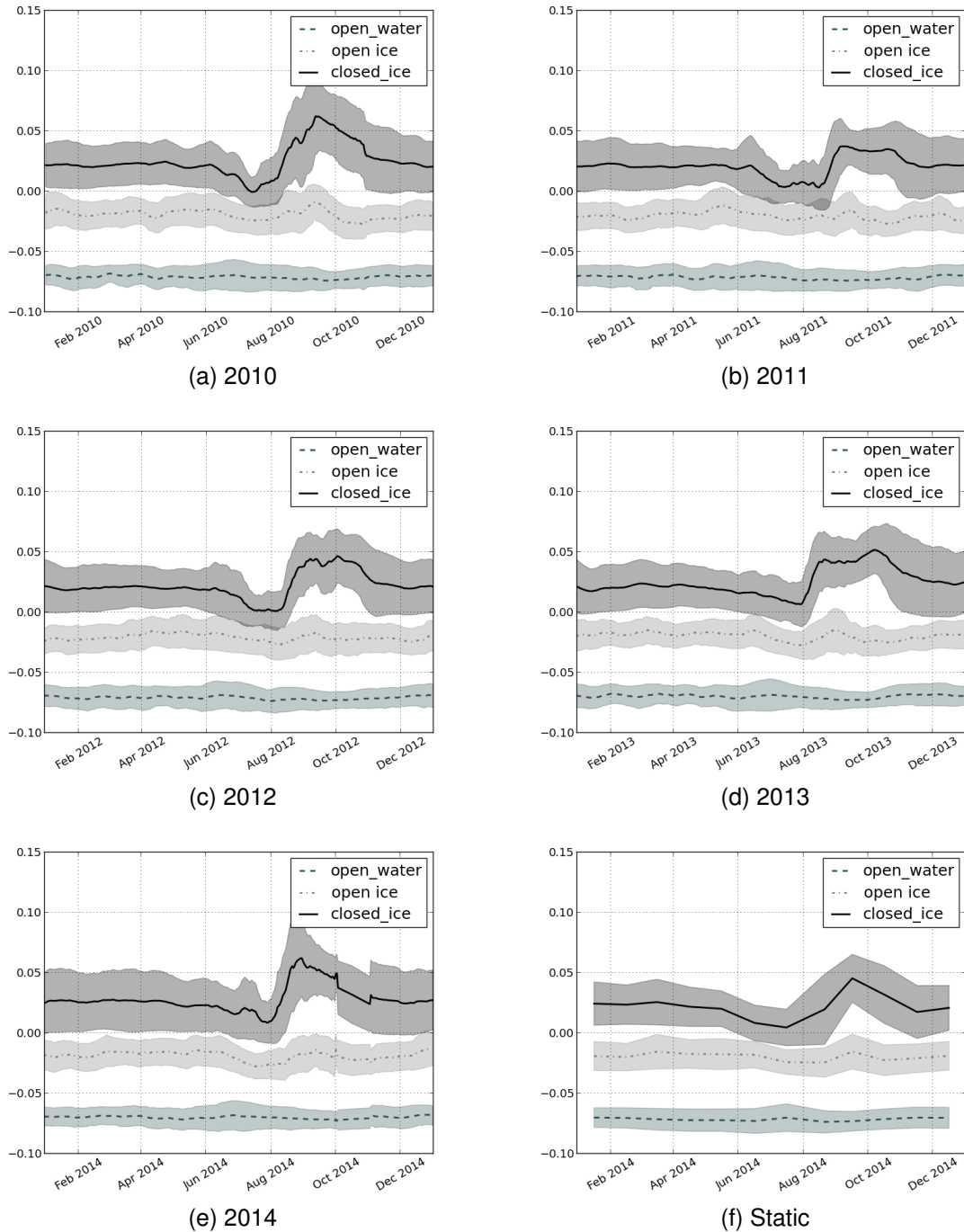


Figure A.3: Dynamical PDF's (mean \pm std) of the SSMIS parameter *GR1937* for *open water*, *open ice*, and *closed ice*, respectively, for the Northern Hemisphere. Statistics are for the year (a) 2010, (b) 2011, (c) 2012, (d) 2013, and (e) 2014. (f) shows the corresponding static PDF's based on a year of data 2007-2008.

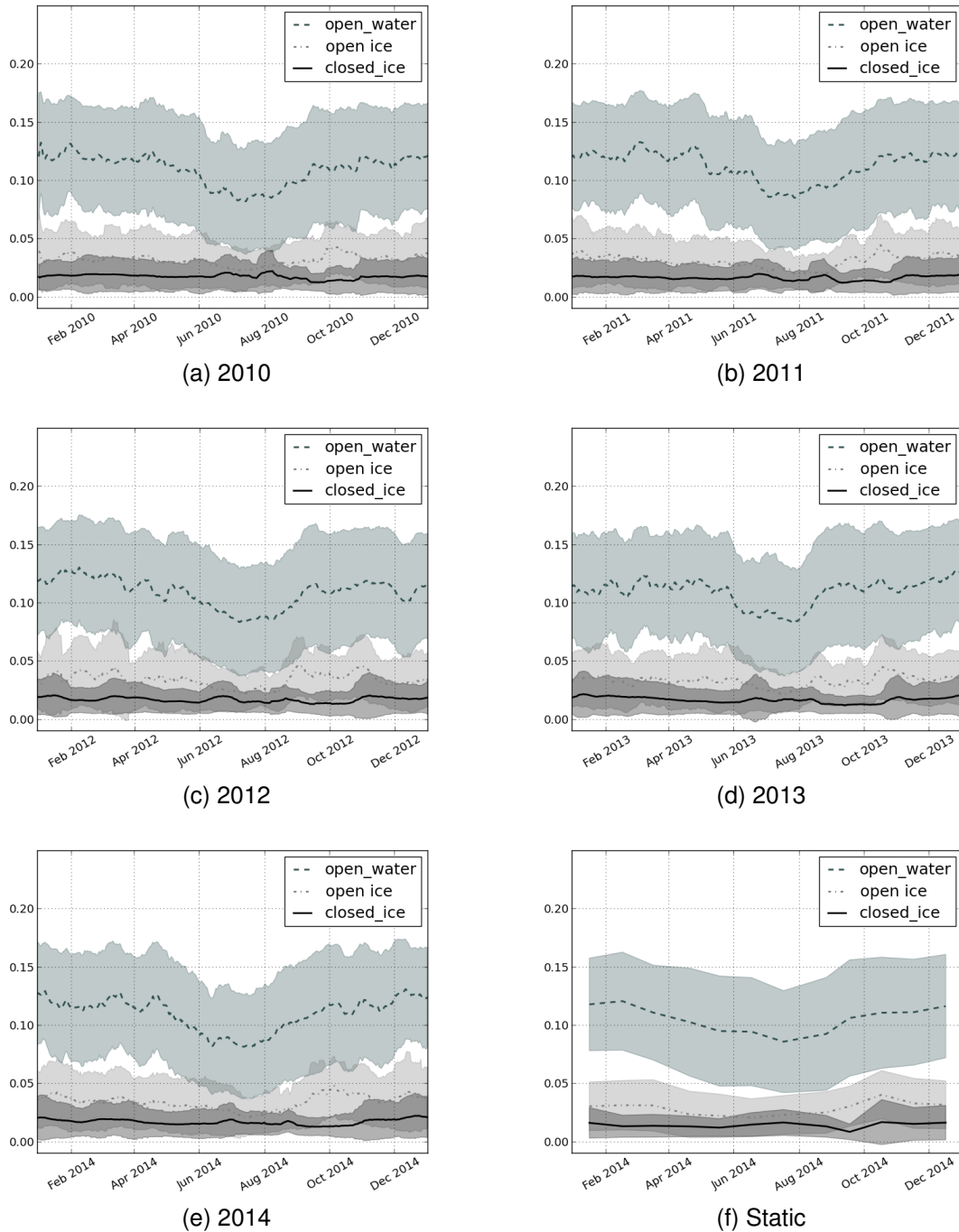


Figure A.4: Dynamical PDF's (mean \pm std) of the ASCAT parameter *anisFMB* for open water, open ice, and closed ice, respectively, for the Northern Hemisphere. Statistics are for the year (a) 2010, (b) 2011, (c) 2012, (d) 2013, and (e) 2014. (f) shows the corresponding static PDF's based on a year of data 2007-2008.

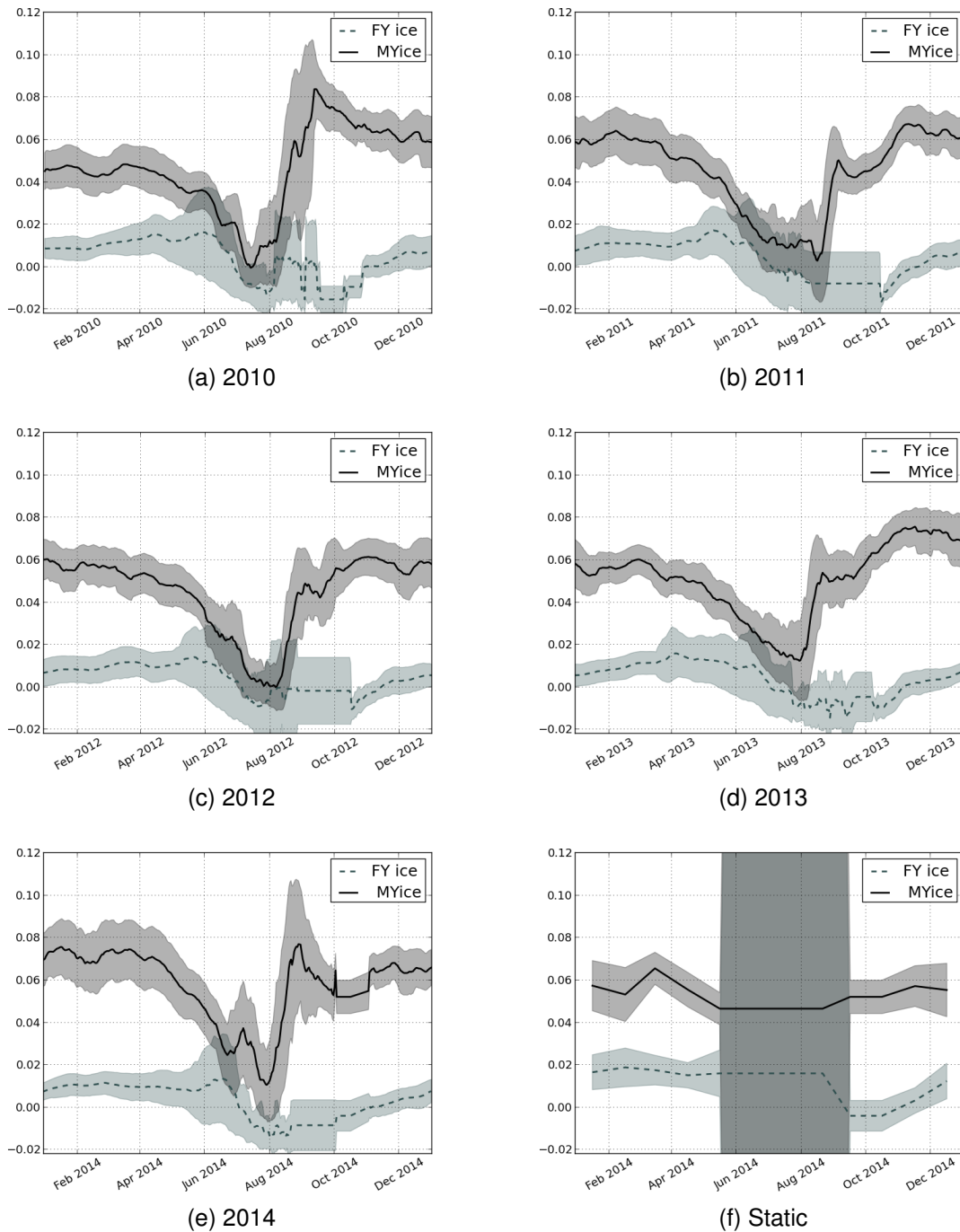


Figure A.5: Dynamical PDF's (mean \pm std) of the SSMIS parameter *GR1937* for first-year ice and multi-year ice, respectively, for the Northern Hemisphere. Statistics are for the year (a) 2010, (b) 2011, (c) 2012, (d) 2013, and (e) 2014. (f) shows the corresponding static PDF's based on a year of data 2007-2008.

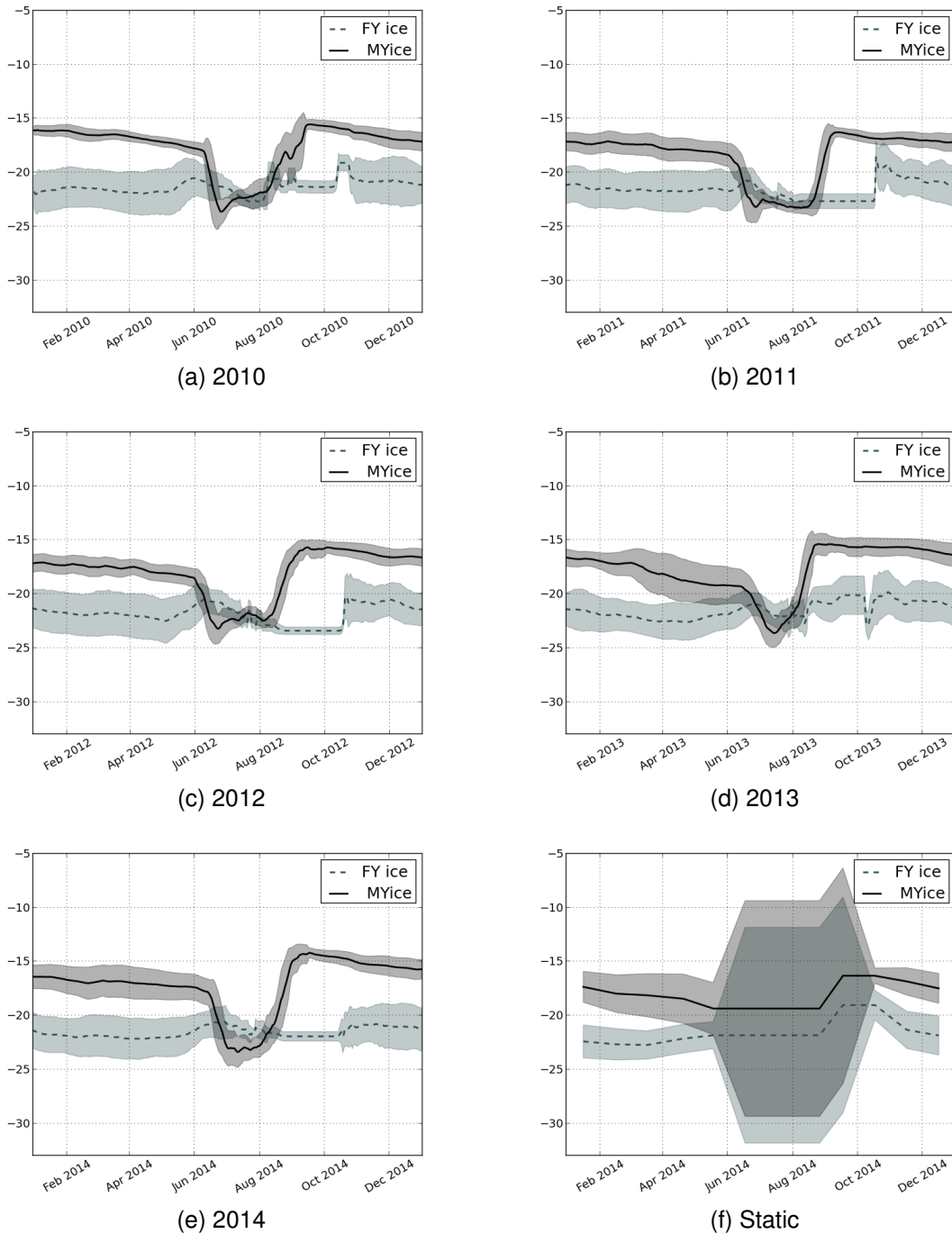


Figure A.6: Dynamical PDF's (mean \pm std) of the ASCAT parameter *bscatt* for first-year ice and multi-year ice, respectively, for the Northern Hemisphere. Statistics are for the year (a) 2010, (b) 2011, (c) 2012, (d) 2013, and (e) 2014. (f) shows the corresponding static PDF's based on a year of data 2007-2008.

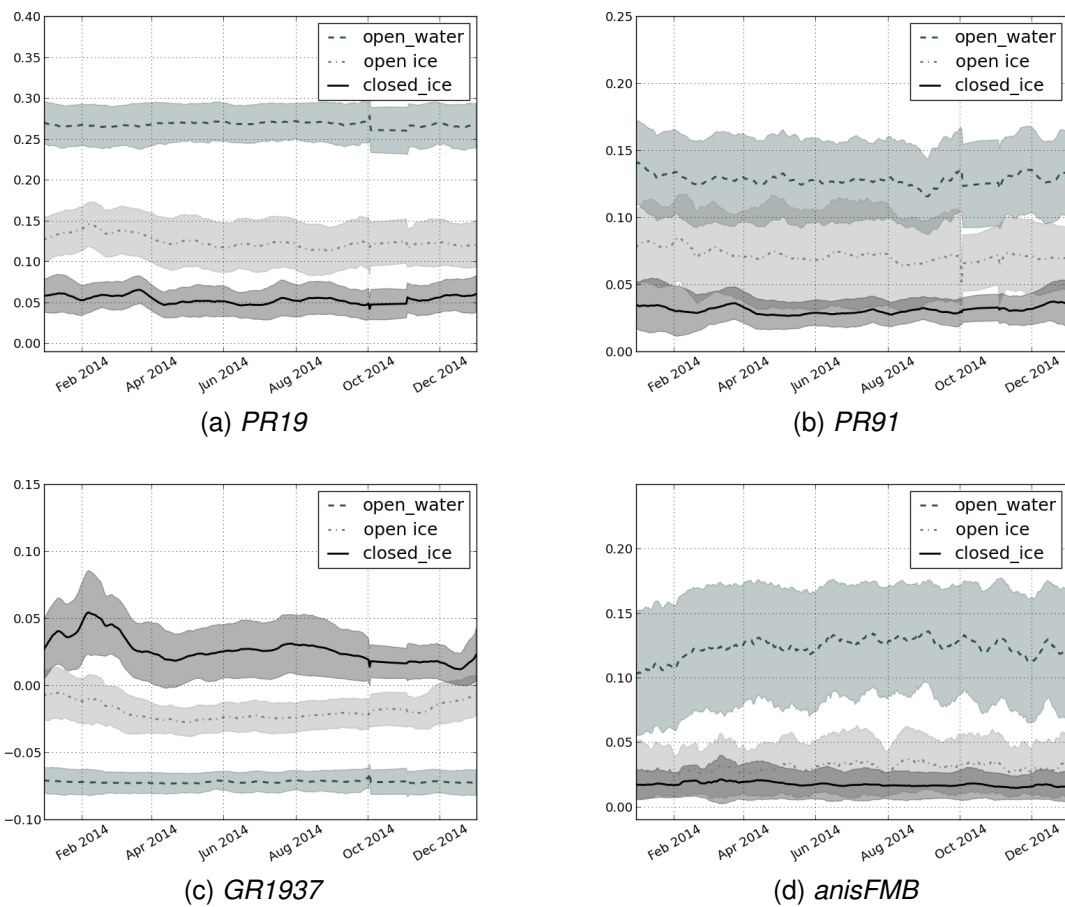


Figure A.7: Dynamical PDF's (mean \pm std) of the parameters for *open water*, *open ice*, and *closed ice*, respectively, for the Southern Hemisphere. Statistics are for the parameters (a) *PR19*, (b) *PR91*, (c) *GR1937*, and (d) *anisFMB*.

B. Flow charts

The following three flow charts give an overview over the processing steps described in section 3. Figures B.1 and B.2 show the processing going from Level 1 (L1) swath data to Level 3 (L3) daily gridded data for scatterometer and PMW data, respectively. Figure B.3 shows the multi-sensor analysis using the individual L3 data parameters as input data to archive the final sea ice products of edge and ice.

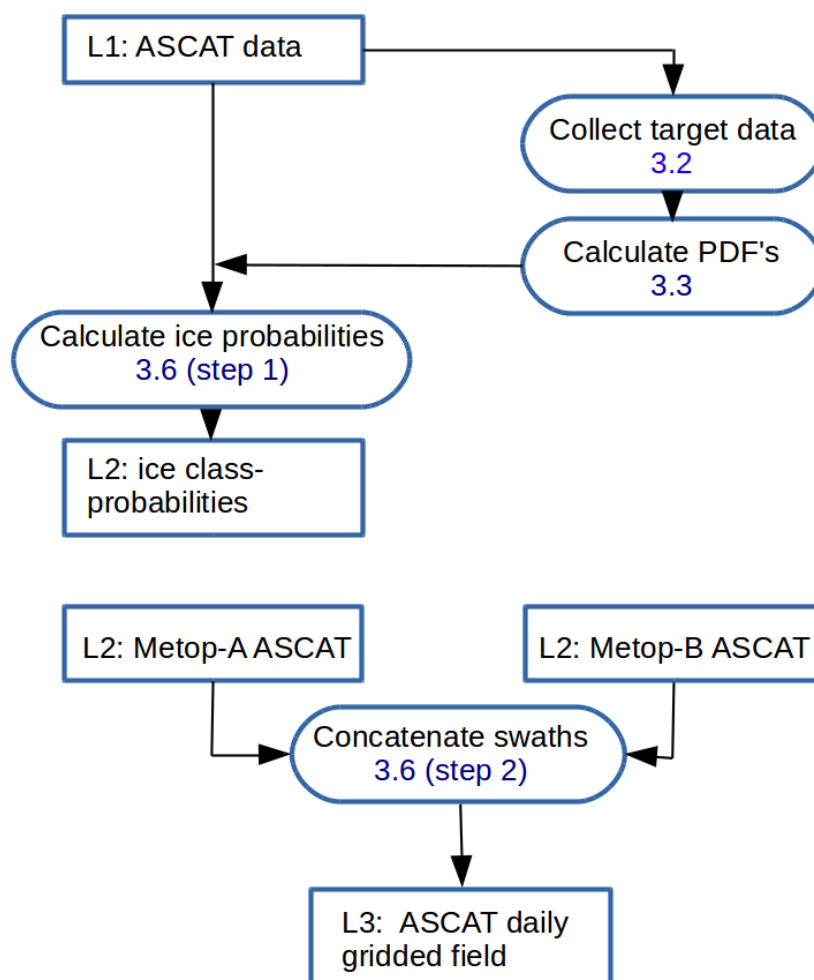


Figure B.1: Flow diagram for ASCAT going from L1 swath data to L3 daily gridded field. References in *blue* refer to sections/equations in the report where the process is described.

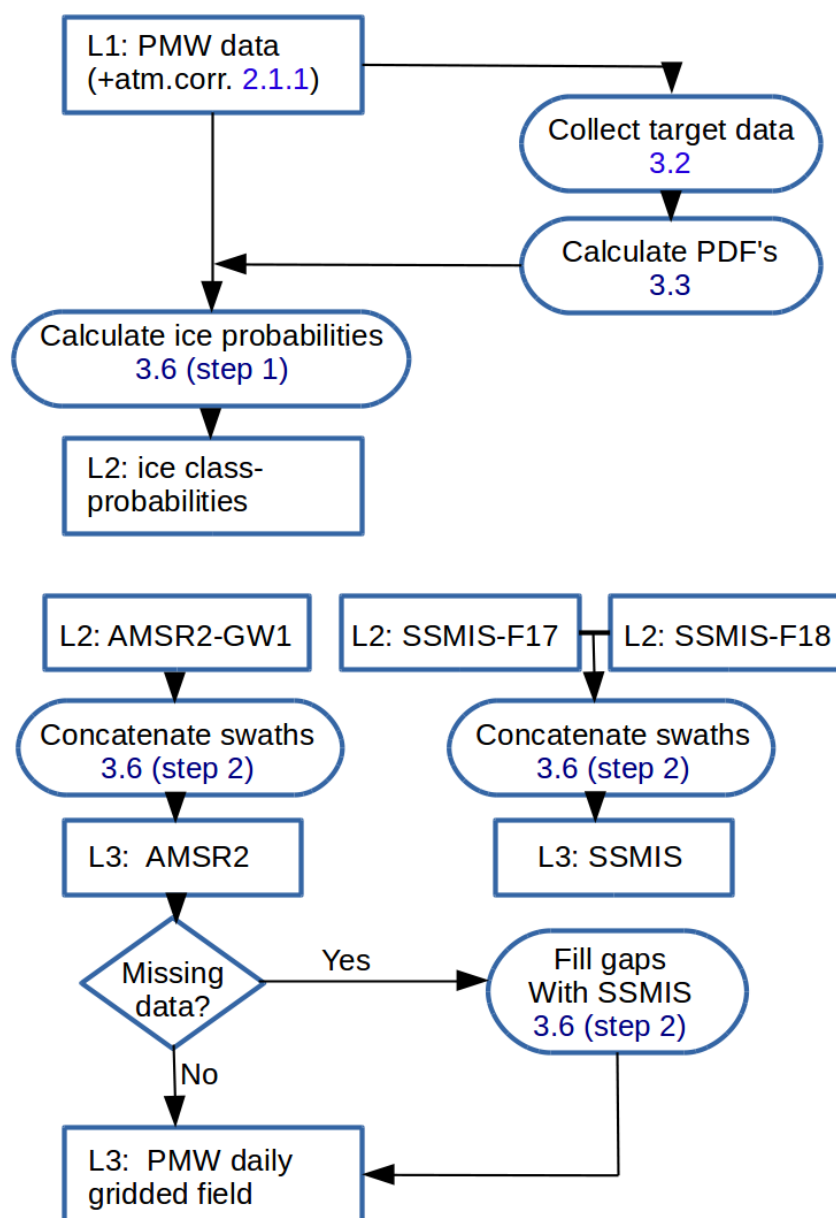


Figure B.2: Flow diagram for PMW going from L1 swath data of both SSMIS and AMSR2 to a L3 daily gridded PMW field. References in *blue* refer to sections/equations in the report where the process is described.

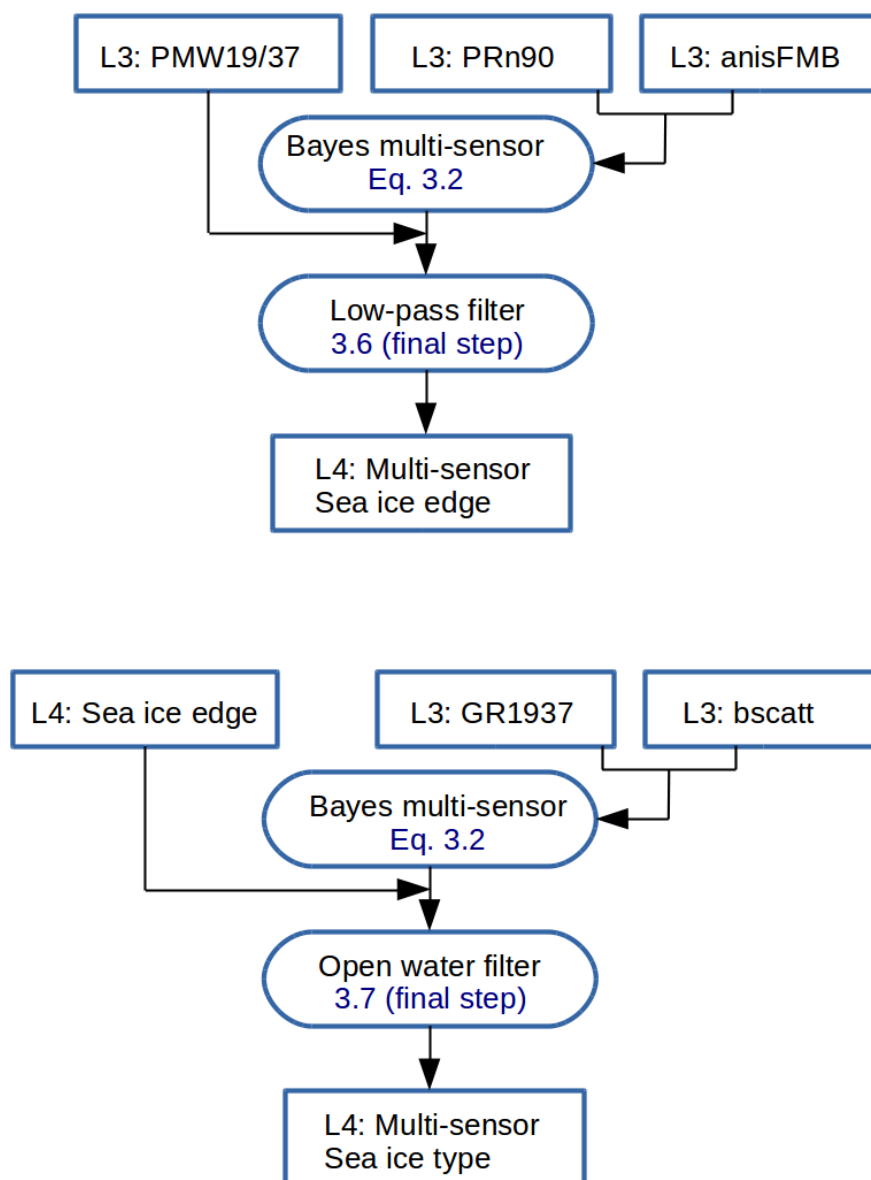


Figure B.3: Flow diagram for the multi-sensor analysis for sea ice edge and sea ice type, respectively. References in *blue* refer to sections/equations in the report where the process is described.

References

- Aaboe, S., Breivik, L.-A., Sørensen, A., Eastwood, S., and Lavergne, T. (2016). Product User's Manual for the OSI SAF Global Sea Ice Edge (OSI-402-b) and Type (OSI-403-b) product – v1.3. EUMETSAT OSI SAF – Ocean and Sea Ice Sattelite Application Facility. <http://osisaf.met.no/docs/>.
- Aaboe, S., Eastwood, S., Lavergne, T., Nielsen, E., and Tonboe, R. (2013). Validation of change from SSMI/I to SSMIS for Global Sea Ice products – v1.1. Technical Report SAF/OSI/CDOP2/MET-Norway/TEC/RP/207, EUMETSAT OSI SAF – Ocean and Sea Ice Sattelite Application Facility. <http://osisaf.met.no/docs/>.
- Andersen, S. (1998). Monthly Arctic sea ice signatures for use in passive microwave algorithms. DMI Technical Report 98-18, Danish Meteorological Institute. <http://osisaf.met.no/docs/>.
- ASCAT Product Guide (2015). EUM/OPS-EPS/MAN/04/0028, issue v5. Available at: <http://www.eumetsat.int>.
- Breivik, L.-A. and Eastwood, S. (2009). Upgrade of the OSI SAF Sea Ice Edge and Sea Ice Type products – Introduction of ASCAT. Technical report, EUMETSAT OSI SAF – Ocean and Sea Ice Sattelite Application Facility. <http://osisaf.met.no/docs/>.
- Breivik, L.-A., Eastwood, S., Godøy, Ø., Schyberg, H., Andersen, S., and Tonboe, R. (2001). Sea Ice Products for EUMETSAT Satellite Application Facility. *Canadian Journal of Remote Sensing*, 27(5).
- Breivik, L.-A., Eastwood, S., and Lavergne, T. (2012). Use of C-Band Scatterometer for Sea Ice Edge Identification. *IEEE Transactions on Geoscience and Remote Sensing*, 50(7):2669 – 2677.
- Breivik, L.-A. and Schyberg, H. (1998). Scatterometer data for saf sea ice products. *Proc. Joint ESA-Eumetsat Workshop on Emerging Scatterometer Applications – From Research to Operations*.
- Cavalieri, D., Germain, K. S., and Swift, C. (1995). Reduction of weather effects in the calculation of sea-ice concentration with the DMSP SSM/I. *Journal of Glaciology*, 41(139):455 – 464.
- Cavanie, A., Gohin, F., Quilfen, Y., and Lecomte, P. (1993). Identification of sea ice zones using the AMI-wind: physical bases and applications to the FDP and CERSAT processing chains. In *Proceedings of the Second ERS-1 Symposium : space at the service of our environment, 11-14 October 1993, Hamburg, Germany*, pages 1009 – 1012.

-
- Comiso, J. (1983). Sea ice effective microwave estimates from satellite passive microwave and infrared observations. *Journal of Geophysical Research*, 88(C12):7686 – 7704.
- Eastwood, S., Larsen, K. R., Laverne, T., Nielsen, E., and Tonboe, R. (2011). Product User's Manual for the Global Sea Ice Concentration Reprocessing – v1.3. EUMETSAT OSI SAF – Ocean and Sea Ice Satellite Application Facility. <http://osisaf.met.no/docs/>.
- Gohin, F. and Cavanié, A. (1994). A first try at identification of sea ice using the three beam scatterometer of ers-1. *International Journal of Remote Sensing*, 15(6):1221 – 1228.
- Kern, S. (2004). A new method for medium-resolution sea ice analysis using weather-influence corrected Special Sensor Microwave/Imager 85 GHz data. *International Journal of Remote Sensing*, 25(21):4555 – 4582.
- OSI SAF project team (2014). OSI SAF CDOP-2 Service Specification Document – v2.3. EUMETSAT OSI SAF – Ocean and Sea Ice Satellite Application Facility. SAF/OSI/CDOP2/M-F/MGT/PL/2-003. <http://www.osi-saf.org/>.
- Steffen, K., Cavalieri, D., Comiso, J., Germain, K. S., Gloersen, P., Key, J., and Rubinstein, I. (1992). The estimation of geophysical parameters using passive microwave algorithms. In Carsey, F., editor, *Microwave remote sensing of sea ice.*, chapter 10, pages 243 – 259. American Geophysical Union. Washington, D. C.
- Tonboe, R. and Lavelle, J. (2015). The EUMETSAT OSI SAF Sea Ice Concentration Algorithm (OSI-401-b) – Algorithm Theoretical Basis Document – v1.4. Technical Report SAF/OSI/CDOP2/DMI/SCI/MA/189, EUMETSAT OSI SAF – Ocean and Sea Ice Satellite Application Facility. <http://osisaf.met.no/docs/>.
- Wentz, F. (1997). A well-calibrated ocean algorithm for SSM/I. *Journal of Geophysical Research*, 102(C4):8703 – 8718.
- www: Reporting Climate Science (2014). <http://www.reportingclimatescience.com/news-stories/article/nsidc-reports-multiyear-arctic-sea-ice-growth.html>.